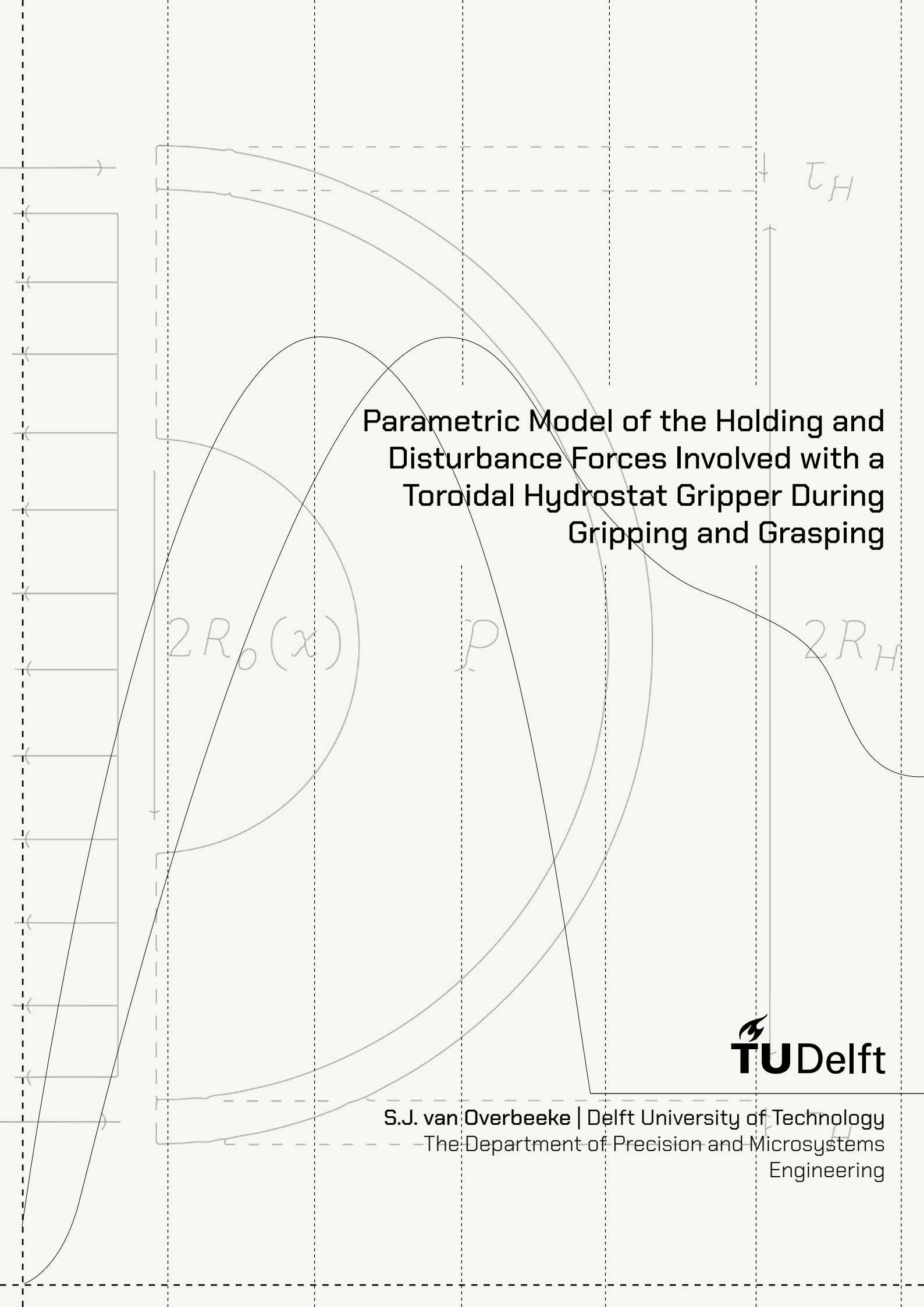

Parametric Model of the Holding and Disturbance Forces Involved with a Toroidal Hydrostat Gripper During Gripping and Grasping

S.J. van Overbeeke | Delft University of Technology
The Department of Precision and Microsystems Engineering

Parametric Model of the Holding and Disturbance Forces Involved with a Toroidal Hydrostat Gripper during Gripping and Grasping

by

S.J. van Overbeeke

to obtain the degree of Master of Science

at the Delft University of Technology,

to be defended publicly on Friday July 5, 2024 at 15:00 PM.

Student number: 4384695

Project duration: May 1, 2022 – July 5, 2024

Thesis committee: Prof. dr. ir. J. Herder, TU Delft
Ir. A. Huisjes, TU Delft, supervisor

TU Delft

Preface

A long journey has come to an end after nearly a decade of studying mechanical engineering. From a young age, I have always loved building just about anything and was very interested to know how and why things work the way they do. Unknowingly, I have always been drawn to engineering. So, pursuing mechanical engineering was a natural choice that perfectly aligned with my interests. Throughout this journey, I have not only learned to be an engineer but also how to tackle challenges in a structured and well-thought-out way. I've realized that this skill extends beyond academics and into many aspects of life.

I would like to thank my supervisor, Ad, for the weekly meetings and his guidance. Most importantly, I want to thank my friends and parents for the breaks, laughs, and their support.

A special thanks to my roommates: Kunal, for his relentless efforts to stop me from procrastinating, and Joop, for his in-house 3D printing business, which has helped me tremendously in building and iterating my manufacturing and test setups. Finally, I want to thank my girlfriend, Helena, who really believed in me and supported me in every way she could.

I am eager to see what the future holds.

Thank you all,

Sander van Overbeeke
Rotterdam, June 2024

Parametric Model of the Holding and Disturbance Forces Involved with a Toroidal Hydrostat Gripper during Gripping and Grasping

S.J. van Overbeeke

The Department of Precision and Microsystems Engineering
Delft University of Technology

Abstract

An earlier study introduced a formula for determining the holding force of a toroidal hydrostat gripper when gripping an object of constant radius, considering a linear stress/strain relationship. However, beyond the holding force, understanding the grasping disturbance force exerted on the object due to the rolling behavior during grip adjustment is crucial to ensure the objects are not damaged or displaced, and are successfully picked up. This study aims to extend the existing model by incorporating the disturbance force for objects with variable radii and using a non-linear stress/strain relationship for the membrane material. A parametric model was developed to estimate these forces as a function of its geometric and material properties. The model was validated through experimental testing and refined using a tuning parameter obtained via optimization algorithms to address parameter uncertainties. The model approximated the holding forces well, with a maximum deviation of 15% at the maximum swallow distance. It overestimated the peak disturbance forces by a factor of 2.5. But when normalized, the force curves showed good resemblance. Surprisingly, the obtained tuning parameter reached a high value of 1.45. as the parameter uncertainties are thought to be less than 20%. This overestimation could be the result of an additional vacuum force, as evidenced by a clear difference in holding force and gripper behaviour is observed in pulling tests for objects with smooth and rough surfaces.

Keywords: soft robotics, hydrostat, gripper, parametric model, grasping

1. Introduction

Lifting objects is a fundamental task in many industries, ranging from manufacturing (1) to food processing (2). The advent of soft robotics has revolutionized this task by enabling more adaptable and gentle handling of delicate items (3)(4). Soft robotic grippers, with their ability to maintain a constant pressure distribution along the object's surface, are particularly beneficial in applications requiring gentle touch. However, they have notable limitations: they often have very low stiffnesses, actuation is a major challenge (5), usually struggle to achieve optimal grasping performance (6), and typically have low holding forces (7)

In contrast, the hydrostat gripper offers significant advantages. This innovative device can achieve high holding forces exceeding $50N$. Unlike traditional soft robotic grippers, the hydrostat gripper eliminates sliding during the gripping process, relying instead on rolling contact. This mechanism minimizes friction forces and can be conceptualized as a soft robotic gripper with an infinite number of gripping fingers, providing superior stiffness and holding capability. Additionally, this gripper is extremely easy to actuate. As a result, it combines the benefits of soft robotics, such as low or zero pressure gradients, with easy actuation and moderate to high holding forces.

The hydrostat gripper consists of a toroidal membrane inflated with a fluid (hydrostat) and operates with two degrees of freedom (DOF), allowing it to move internally relative to the exterior structure.

(a) Hydrostat gripper with hand-held device holding a cup.

(b) Hydrostat gripper with hand-held device holding a bottle.

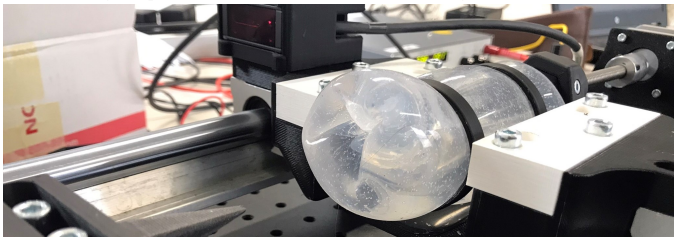

(c) Hydrostat gripper in the experimental test.

Figure 1: A two-degree-of-freedom soft toroidal hydrostat gripper. The inner and outer membranes can be actuated independently by the blue pen and white casing, respectively.

It grasps objects by actuating the outer membrane relative to the inner membrane, effectively rolling the hydrostat over the object. The applied hydrostatic pressure ensures a secure and stable grip, adapting to the object's shape. Figure 1 illustrates the gripper, where the blue pen actuates the inner membrane, and the white casing actuates the outer membrane of the hydrostat.

Current state-of-the-art technology (8)(9) has already determined the holding force for objects with a constant radius. However, when lifting objects, the act of grasping and the forces involved are equally important. Proper force application is crucial in industries like agriculture and food, where products are fragile (7). In some cases, only a specific force can be applied while grasping. For example, when handling a chicken drumstick in a tray, the disturbance force must be lower than the friction force between the chicken and the tray to avoid pushing the object away. This also applies to free-hanging items like berries, tomatoes, and other fruits and vegetables, which have very low normal forces (10).

In the case of the hydrostat gripper, an axial disturbance force is applied on the object while grasping. Understanding the magnitude of this of this force will aid optimizing the gripper's performance.

The objective of this paper is to develop a parametric model that can describe both the holding and disturbances forces of a soft hydrostat gripper handling objects with variable radii, and then validate the model using an experimental test setup.

This paper is structured as follows. In section 2, the theoretical foundation of the proposed model is discussed, including its implementation in Matlab and the setup for validation tests. Section 3 presents the outcomes of the model tuning and experimental tests, providing detailed analysis and data. In section 4, a comprehensive discussion interprets the results, examining their implications and significance. Finally, section 5 offers the conclusions drawn from the study, summarizing key findings and suggesting potential directions for future research.

2. Methodology

2.1. Mathematical Formulation

Root et al. (8) determined a formula of the hydrostat for the holding force onto a cylinder as a function of the initial hydrostat radius R_i, the pressurized hydrostat radius R_H, the initial membrane thickness t_i, the object's radius R_o, the swallowed object length L_o and the material properties E and μ:

$$\frac{F_c}{(ER_it_i)} = 2\pi L_o R_o \mu \left(\frac{1}{R_H R_i} - \frac{1}{R_H^2}\right) \tag{1}$$

We aim to extend this by expressing the axial disturbance force projected onto the object during grasping F_{Dist}, and adjust for an object with a variable radius $R_o(x)$.

The forces acting on the object in both the radial and axial direction can be expressed as follows:

$$F = PA_o \tag{2}$$

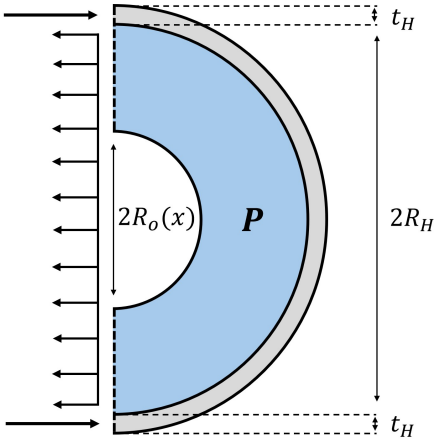

Figure 2: Free Body Diagram of a cross-section of the hydrostat. The grey section represents the silicone membrane of the hydrostat with thickness t_H, while the blue section represents the water contained within the hydrostat. R_H denotes the radius of the hydrostat and R_o represent the radius of the object.

The hydrostatic pressure P can be determined using the thin-walled hoop equation, Hooke's Law and a Poisson's ratio of 0.5.

$$P = ER_it_i \left(\frac{1}{R_H R_i} - \frac{1}{R_H^2}\right) \tag{3}$$

The area A_o can be split into a radial and an axial component:

$$A_{oR} = 2\pi \int_0^{L_o} R_o(x)\, dx \tag{4}$$

$$A_{oA} = \pi R_o^2(L_o) \tag{5}$$

Hooke's law describes a linear relationship between stress and strain with a constant Young's modulus. However, for elastomers like silicone, this is often not the case, as Young's modulus is a function of strain, decreasing as strain increases. For small variations in strain ($\Delta\varepsilon < 0.2$), this does not result in significant differences. However, for larger changes, the modulus and, consequently, the forces will be overestimated.

Combining the formulas give the following equations for the radial force F_R and axial force F_A:

$$F_R = A_{oR}E(\varepsilon)R_it_i \left(\frac{1}{R_H R_i} - \frac{1}{R_H^2}\right) \tag{6}$$

$$F_A = A_{oA}E(\varepsilon)R_it_i \left(\frac{1}{R_H R_i} - \frac{1}{R_H^2}\right) \tag{7}$$

The holding and disturbance forces can be expressed as followed:

$$F_{Hold} = \mu\, F_R - F_A \tag{8}$$

$$F_{Dist} = F_A \tag{9}$$

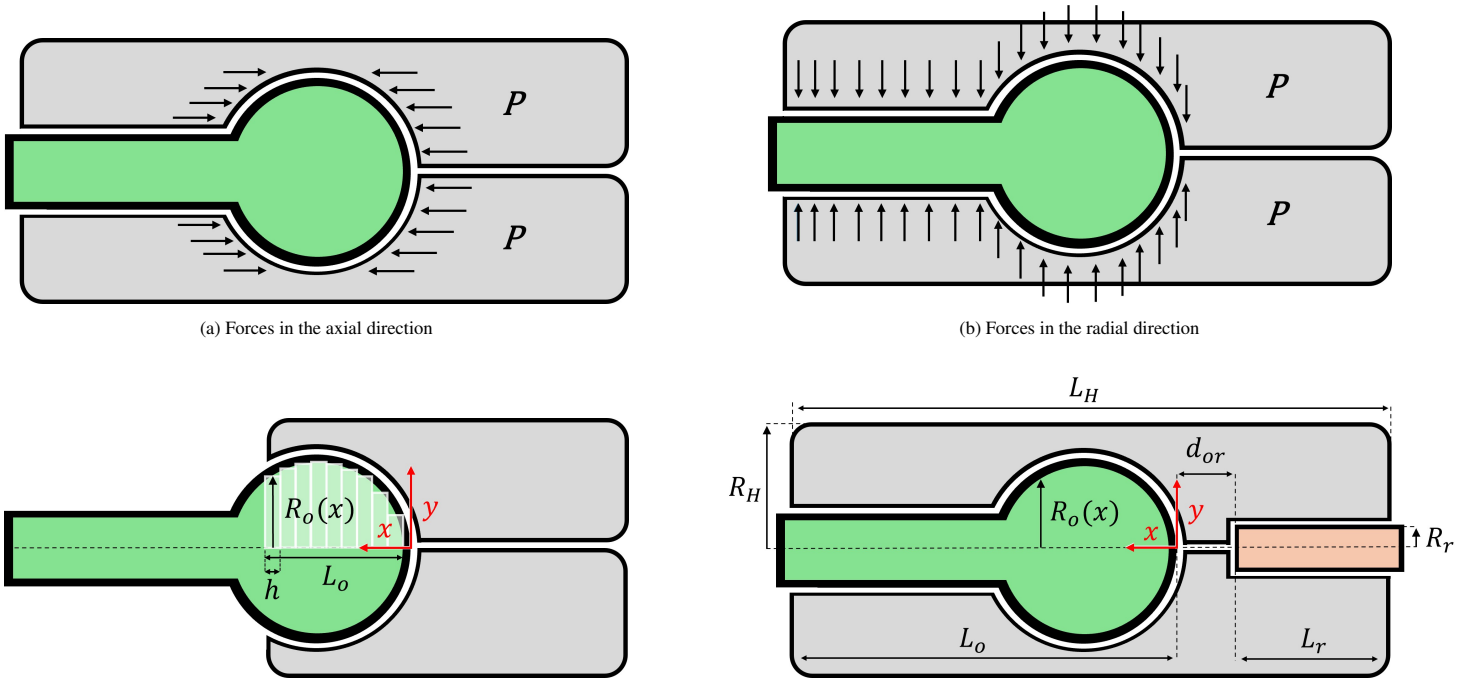

(a) Forces in the axial direction

(b) Forces in the radial direction

(c) Numerical interpretation of A_o

(d) Depiction of the object and the rod in the test setup

Figure 3: Schematic cross-sectional view of the hydrostat, illustrating the hydrostat in grey, the object in green and the actuation rod in orange

2.2. Numerical Implementation

To implement the formulas in Matlab, they must be converted from continuous to discrete equations. The total length of the swallowed object, L_o, is divided into n steps. The area in the radial direction can then be described as follows:

$$A_{oR} = 2\pi h\left(\frac{1}{2}R_o(0) + \sum_{i=1}^{n-1} R_o(ih) + \frac{1}{2}R_o(L_o)\right) \tag{10}$$

Then, at every step, both the radial and axial force are calculated. Additionally, at every step, the new R_H must be determined. Assuming no pressure gradient inside the hydrostat, R_H will be consistent across its entire length. R_H is determined by summing the individual volumes of the unperturbed hydrostat V_{H0}, the actuation rod V_r, and the object V_o, and solving for the cylindrically shaped hydrostat:

$$R_H = \sqrt{\frac{V_{H0} + V_r + V_o}{L_H\,\pi}} \tag{11}$$

2.3. Hydrostat Manufacturing

The hydrostat is constructed by inverting a silicone tube made by smearing SORTA-CLEAR 12 liquid silicone onto a rotating PVC pipe. The rotation ensures that the silicone spreads uniformly and prevents dripping during the curing process. Multiple layers of silicone are applied until the desired thickness is achieved. Once cured, the ends are trimmed, and the tube is inverted, creating a pocket. This pocket is then filled with water under a pressurized tap. When the desired hydrostat radius is reached, the tap is shut off, and the ends are sealed with a zip tie. The tied-off part is then pushed inside the hydrostat, completing the gripper.

2.4. Test Procedures

A hydrostat gripper with parameters $R_i = 16\ mm$, $t_i = 1.4 - 1.6\ mm$, and $L_H = 130\ mm$ is used for the experiment. Instead of using multiple hydrostats with different parameters, a single hydrostat is utilized, and the test objects are scaled. This approach allows for precise manufacturing using a 3D printer.

Two types of tests are conducted: a push test and a pull test. For the push test, the inner membrane of the hydrostat is held in place while the outer membrane is moved forward, rolling the hydrostat over the test object. During this procedure, the axial disturbance force is measured.

For the pull test, the hydrostat is first pushed to the desired length, and then both the inner and outer membranes are pulled back. During this procedure, the axial force is measured.

2.5. Model Parameter Tuning

The model's parameters E, t_i, R_i, R_H and μ cannot be determined with high accuracy. Measuring the thickness of a silicone sleeve with a caliper is not sufficiently precise. To address this, correction factors $C_{1...n}$ can be applied to these parameters, approximating in an overall correction factor C. This factor helps to fine-tune the model, allowing the friction force to be described as follows:

$$F_f \approx C\mu A_{oR} E R_i t_i \left(\frac{1}{R_H R_i} - \frac{1}{R_H^2}\right) \tag{12}$$

When RH remains constant for all steps of n and R_o is a constant, the friction force scales linearly with the swallow distance L_o. According to equation 11, maintaining a constant R_H requires that V_r equals V_o, since V_{H0} is a constant.

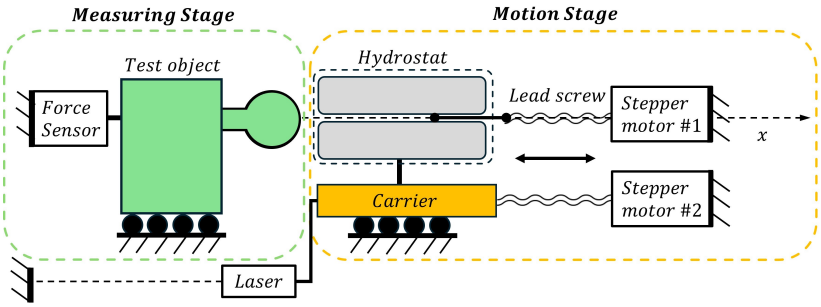

(a) Schematic depiction of the test setup. The motion stage depicted in orange and the measuring stage depicted in green

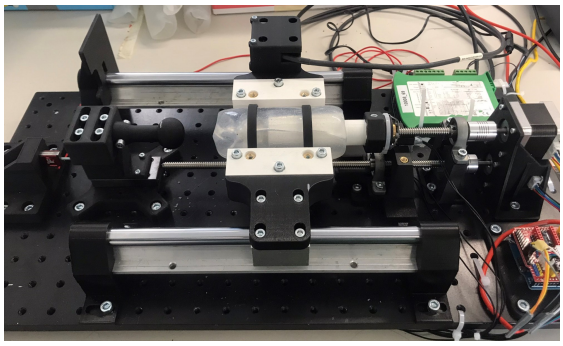

(b) Photograph of the physical test setup, showing the arrangement and integration of the motion and measuring stages, including the Arduino and the measuring device: NI USB 6008 I/O.

Figure 4: Experimental test setup designed as two main components: a motion stage and a measuring stage. The motion stage allows for actuation of the inner and outer membrane of the hydrostat as well as measuring the actuated distance. The measuring stage measures the axial force on the test object in both pulling and pushing motions.

2.6. Test Setup

The aim of the test setup is to measure the axial force, without any disturbances, in pulling and pushing motions as a function of the actuated gripping distance. The test setup is designed as two main components: a motion stage and a measuring stage. Figure 4 depicts both parts, the motion stage in red and the measuring stage in green.

The motion stage consists of a carrier which sits on top of a linear guide system, to allow for a purely axial movement in the x-direction, and two stepper motors that can individually actuate the hydrostat's inner and outer membrane. The hydrostat is suspended in the carrier and is achieved using compliant rings of various diameters, ensuring the hydrostat's center remains aligned with the internal actuator. Additionally, a Micro-Epsilon ILD1420-100 laser mounted on top of the carrier measures the distance in real time.

The measuring stage consists of the test piece positioned on a linear slider (RTS 2065), which permits only pure sliding motion with negligible friction forces. Consequently, the forces measured are solely those exerted by the hydrostat. This slider is connected to a Futek LSB200 load cell capable of measuring both pulling and pushing forces.

3. Results

Multiple tests were conducted. Figure 5 depicts the different test objects that were used, all objects had the same length. To ensure consistency, the hydrostat was set in the carrier and its position was not changed throughout all tests. Additionally a starting point was set from where the hydrostat would start all the tests. For this starting point the hydrostat was positioned as close as possible to the test piece without contact, ensuring no prestress on the load cell. Furthermore, the distance between the object and the actuation rod d_{or} was kept as short as possible at 10 *mm*.

3.1. Pull Tests

Two types of objects were measured during the pull tests; the cylinder and the spheres. The pull tests were conducted as follows: the hydrostat would be brought to the starting point, the outer membrane would be actuated to the required distance, then the pull test was initiated by pulling both the inner and outer membrane at a speed of 100 mm/min and the axial force was measured.

This resulted in data sets such as figure 6, where positive forces indicate the compressive forces on the load cell. This illustrates that, upon initiating the pull test, a compressive force is acting on the load cell. This occurs due to the axial force F_A exerting a force on the top part of the cylinder. As the pull test progresses, the force steadily decreases until it reaches its minimum, which is the maximum holding force F_{Hold}. According to equation A.16, the difference between the initial compressive force and the maximum holding force is the friction force $F_R\,\mu$. This friction force was then calculated and used for further analysis, allowing for the separate assessment of the radial and axial forces.

3.1.1. Cylinder: Model Tuning

The holding forces were measured for the cylinder, for swallow distances of 20, 30, 40 *mm*. Two tests were conducted per swallow distance and the mean value was computed. Following this, a first-order function was fitted through the three mean data points. Figure 7 showcases the expected linear relationship between force and displacement excellently.

The curve intersects the x-axis at $x = 10.09$. This intersec-

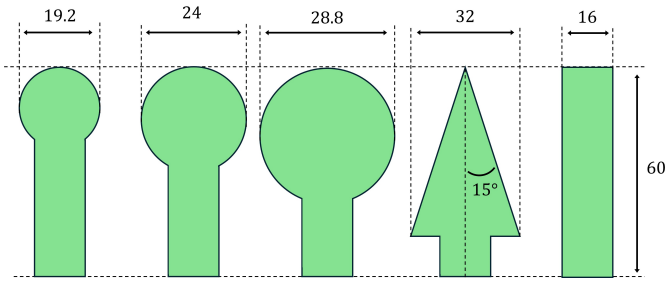

Figure 5: Test Objects: from left to right; 80% sphere, 100% sphere, 120% sphere, cone, cylinder. All values are in *mm*.

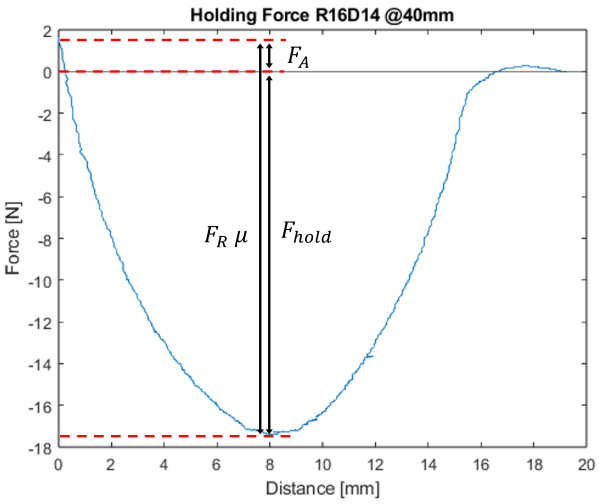

Figure 6: Force vs displacement for a single pull test. F_A represents the axial disturbance force, $F_R\ \mu$ indicates the maximum friction force, and F_{hold} denotes the maximum holding force.

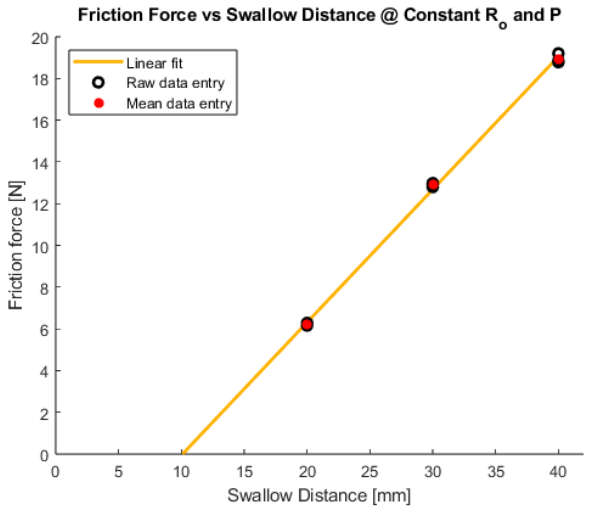

Figure 7: Friction force at constant hydrostat and object radius. Showcasing that the measured data aligns with the predicted linear relationship between friction force and swallow distance.

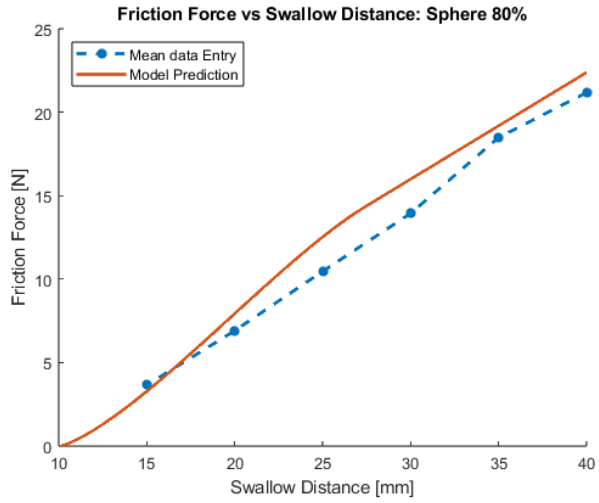

(a) Friction force Sphere scaled 80%

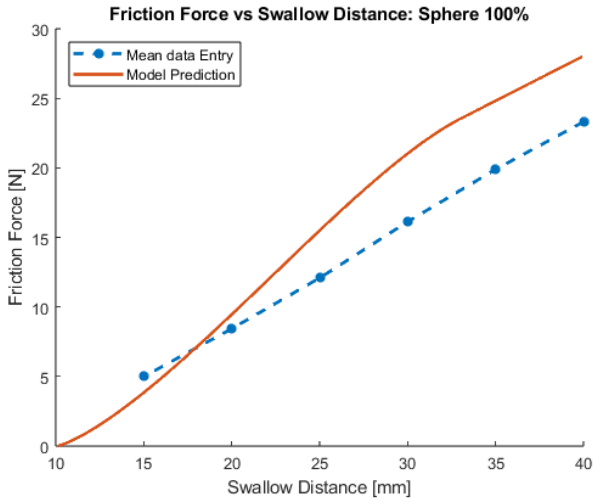

(b) Friction force Sphere scaled 100%

Figure 8: Friction force for spheres scaled at 100% and 80%, obtained during pull tests. The distance offset is applied to the data to align with the model prediction.

tion indicates the zero gripping point, beyond which gripping begins. Figure 12 shows that this value represents the initial distance between the object and the hydrostat's tip, resulting from misalignment, plus the distance from the tip to the zero gripping point, due to the curvature of the hydrostat's tip.

Utilizing an optimization algorithm and incorporating the newly identified distance offset, the model was fitted against the obtained curve, resulting in a coefficient value of $c = 1.4$, with a corresponding minimization function value of 1.26×10^{-8}.

3.1.2. Sphere

Two scaled versions of the sphere were examined at 100% and 80%. The holding force was measured at intervals of 15, 20, 25, 30, 35, and 40 *mm* swallow distance. Friction force was determined and at each interval, the mean value of three data points was calculated and depicted in figure 8. Note that the model's entry in the figure is adjusted along the x-axis with the distance offset parameter and starts at $x = 10.09$. The model shows great agreement with the measure data in magnitude, with only a maximum deviation of 15% at the maximum swallow distance. However, the data entry of the 100% sphere seems a bit more linear than anticipated by the model.

3.2. Push tests

A series of push tests were conducted. Unlike the pull tests, which involved separate measurements for each swallow distance, the push tests allowed for one continuous measurement. The hydrostat was brought to the starting point, and then the outer membrane of the gripper was actuated and rolled over the object for 50 *mm* at a speed of 100 *mm*/*min*, and the axial force was measured. For each test object, three measurements were taken, and the mean value was used for analysis. Due to

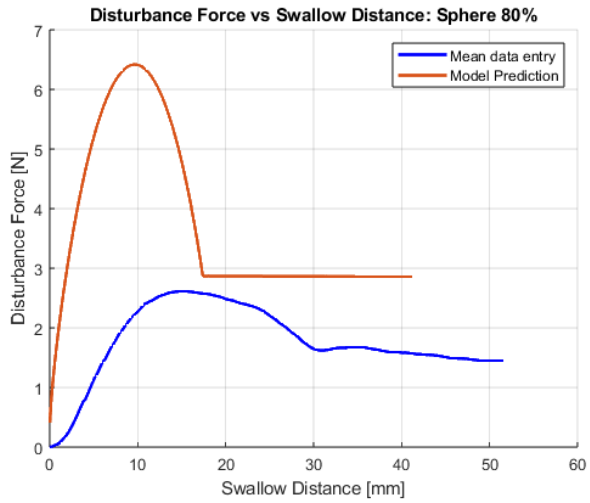

(a) Axial disturbance force vs. Swallow Distance for Sphere at 80% Scale.

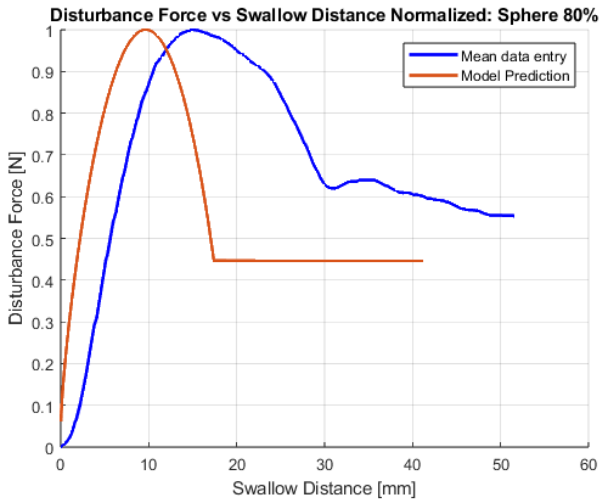

(b) Normalized Axial disturbance force vs. Swallow Distance for Sphere at 80% Scale.

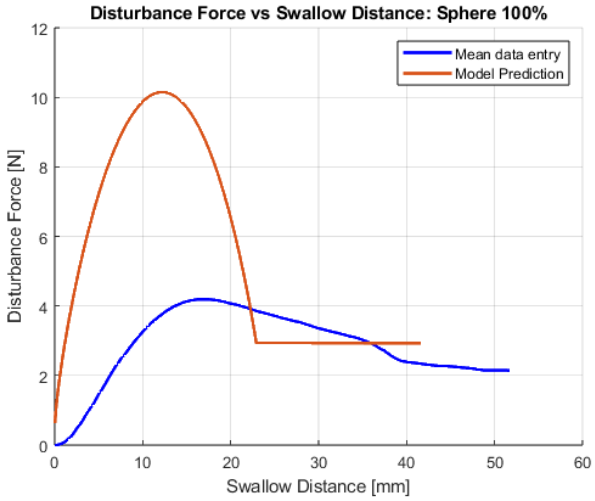

(c) Axial disturbance force vs. Swallow Distance for Sphere at 100% Scale.

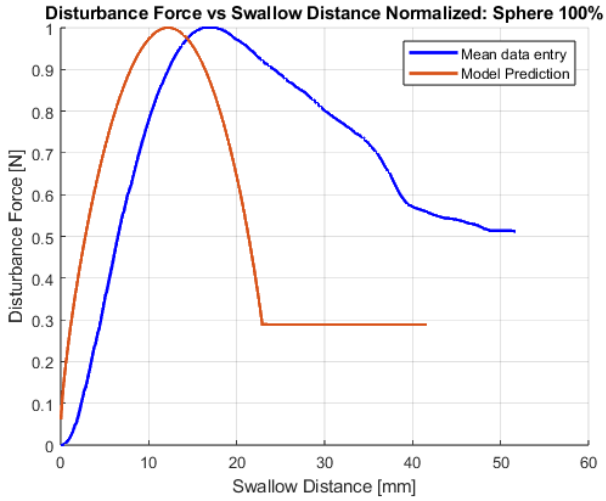

(d) Normalized Axial disturbance force vs. Swallow Distance for Sphere at 100% Scale.

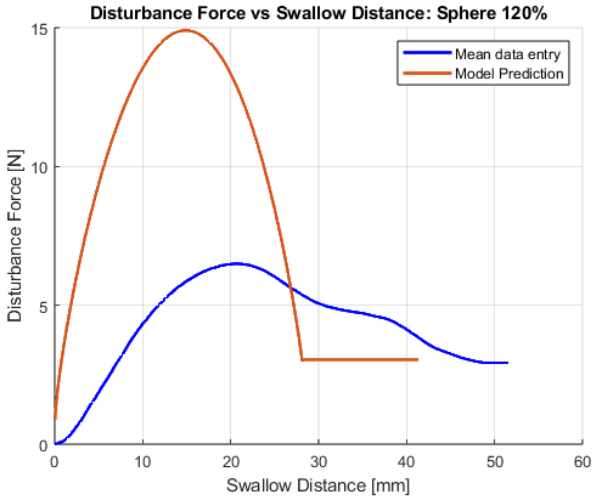

(e) Axial disturbance force vs. Swallow Distance for Sphere at 120% Scale.

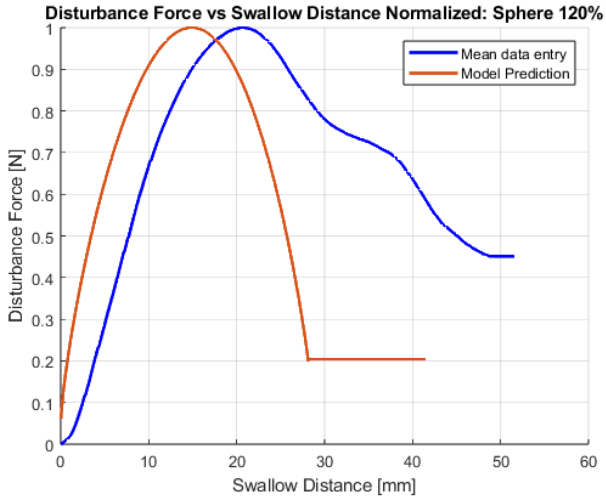

(f) Normalized Axial disturbance force vs. Swallow Distance for Sphere at 120% Scale.

Figure 9: Axial disturbance force vs. swallow distance for three scaled spheres obtained during push tests. The model overestimates the disturbance force by a factor of 2.5. A normalized figure is included to highlight the resemblance between the two curves. The discrepancy between the swallow distances of the data and the model is due to the distance offset observed during model tuning. The offset between the peaks is likely an effect of the distance offset.

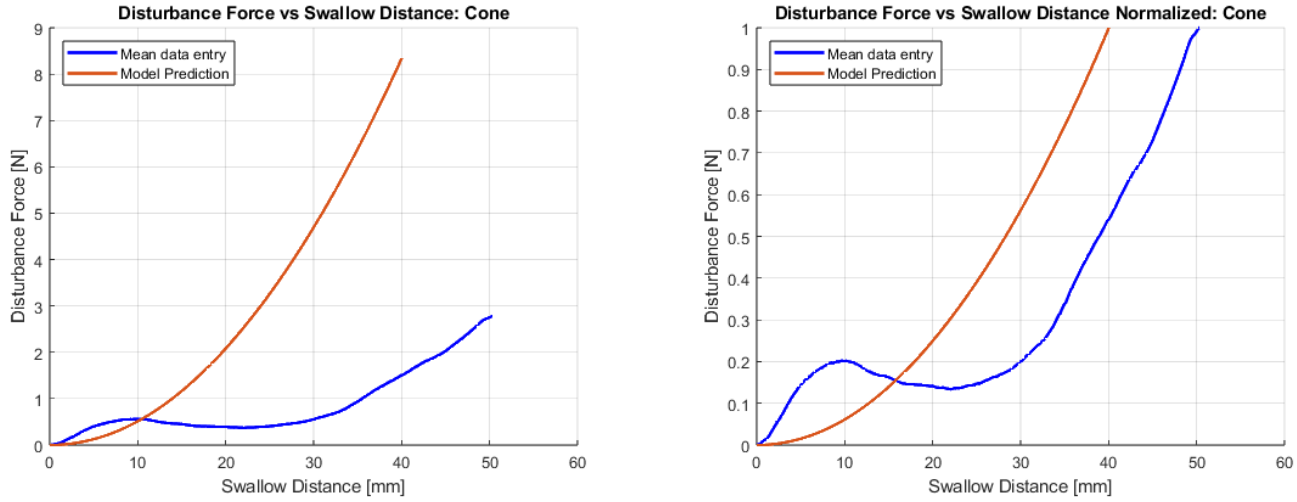

(a) Axial disturbance force cone shape.

(b) Normalized axial disturbance force cone shape, showing a similar slope.

Figure 10: Axial disturbance force vs. swallow distance for a cone shape obtained during push tests. The model overestimates the disturbance force by a factor of 3, so a normalized figure is included to highlight the resemblance between the two curves. The discrepancy between the swallow distance of the data and the model is due to the distance offset observed during model tuning.

the measured axial force exceeding the predicted model values, two figures are presented for each object: the actual measurement and a normalized figure, where both curves are divided by their respective maximum values. It is important to note that due to the previously identified distance offset, the lengths of the model prediction and the data entry curves differ by a value of 10.09. Ideally, the model prediction should be stretched or translated to match the length of the data entry. However, since it is unclear where in the curve these adjustments should be made, the model prediction remains unstretched.

3.2.1. Sphere

Three scaled versions of the sphere were tested: 80%, 100%, and 120%, as depicted in figure 9. Across all spheres, the magnitude of the peak disturbance force is overestimated by approximately 2.5 times. The normalized figure, however, shows a good resemblance between the two curves, particularly in the initial rise. Although the peaks are slightly offset, this is likely due to the distance offset. After the peak, the measured data does not descend as quickly as the model prediction, which is attributed to imperfect wetting of the sphere. Figure 12c illustrates that the hydrostat struggles to follow the shape of the sphere when its radius decreases rapidly. However, when the hydrostat is actuated further, it eventually conforms to the shape in a rapid manner. This behavior is reflected in the graphs for all three scaled versions of the sphere, but it is most notable in figure 9f, where after the peak a descent is followed by a stall at 30 *mm*, and then another rapid descend. Finally, all three versions reach a relatively constant value when they transition to the cylindrical part of the object after the sphere, which is also reflected in the model prediction.

3.2.2. Cone

The cone shape depicted in figure 10 overestimates the peak disturbance force by a factor of 3. The normalized figure, however, shows that the data and the model experience a similar hyperbolic shape. The initial bump and dip in the data are caused by a slight initial misalignment between the hydrostat and the cone, along with a small initial gap at the beginning of the hydrostat. Figure 12a demonstrates that the hydrostat can sometimes start at a slight angle, causing a higher initial axial force that dissipates once the hydrostat aligns with the object. Additionally, the model assumes no gap inside the hydrostat, but in reality, there is a small hollow section that dissipates slowly when actuated. This results in no initial contact between the object and the hydrostat, causing the slight dip in the curve.

3.2.3. Disturbance Force at Different Distances Between the Object and Actuation Pen

Figure 11 shows that the distance between the object and the actuation rod d_{or}, significantly impacts both the maximum disturbance force and the shape of the curve. Figure 11a illustrates the disturbance force for d_{or} values of 10 and 50 *mm*. This variation results in a 25% increase in the peak disturbance force and a 50% increase in the resting force at 40 *mm* swallow distance.

4. Discussion

4.1. Measuring Difficulties

The soft nature of the hydrostat introduced some measurement errors. Notably, there was some variation in measurements when the hydrostat's position relative to the carrier changed. When the hydrostat remained stationary, the results were very consistent. However, when the hydrostat was rotated or the distance d_{tc} was altered, the measurements could differ slightly. This variation was most pronounced during the push tests, where differences in hydrostat-object alignment significantly impacted the peak disturbance force by up to 1 *N*. Thus, it was crucial

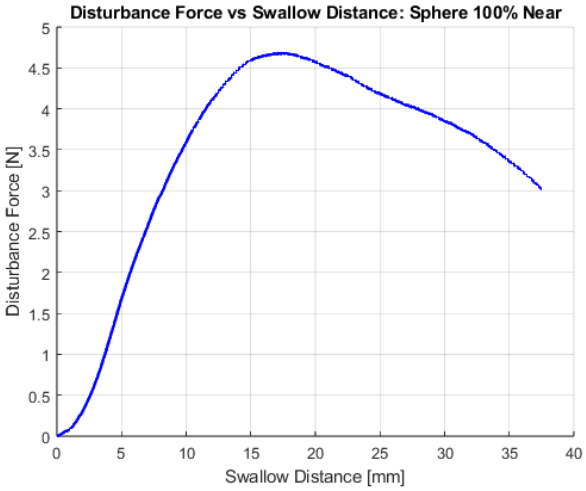

(a) Axial disturbance force at an object-pen distance of 10 *mm*

(b) Axial disturbance force at an object-pen distance of 50 *mm*

Figure 11: Axial disturbance force on a 100% sphere for both small and large distances between the object and actuation pen, demonstrating that both the peak disturbance force and the disturbance force at maximum swallow distance are higher for smaller distances.

to keep the hydrostat in the same position during all measurements.

Even with the hydrostat's position relative to the carrier kept constant, changes in the distance between the object and the actuation rod d_{or} affected the disturbance force. Increasing distance d_{or} resulted in a significant drop in disturbance force. In the model, the part between the object and the actuation rod is assumed to be fully rigid. However, this is not entirely accurate, as this part is made of silicone and can be interpreted as a spring with unknown properties. This spring constant has an inversely proportional relationship with distance d_{or}, where increasing distance d_{or} would decrease the spring constant and vice versa. To minimize its effect, all measurements were conducted with the smallest distance d_{or} possible, ensuring this part was as rigid as possible. Generally, for gripping applications, minimizing the disturbance force is desired, and therefore a larger distance d_{or} is recommended.

Unlike the push tests, the pull tests were quite consistent throughout, regardless of the hydrostat's orientation or d_{or}.

4.2. Distance Offset

During model tuning, a distance offset became apparent, revealing a discrepancy between the actuated and true swallow distance. This offset is attributed to two main factors: the initial misalignment between the hydrostat and the test object, and the slight overhang of the hydrostat due to its tip curvature. The hydrostat is not a rigid object, and figure 12a shows that it sometimes curves away from the center. This curvature depends significantly on how the hydrostat hangs in the carrier, both in rotation and in the distance between the tip of the hydrostat and the carrier, denoted by d_{rc}. To avoid pre-loading the load cell during tests, a distance between the hydrostat and the object d_{ot} is introduced.

Additionally, figure 12b shows that the tip of the hydrostat curves upwards, creating a small distance d_{tw} between the tip and the point where the actual wetting of the object begins. This offset decreases when objects with larger radii are gripped.

Due to the adjustment of the distance offset, the curves of the data and the model prediction during the push tests are no longer equal in length. Ideally, the model prediction should be stretched or shifted along the distance axis to account for this. The main reason for the distance offset is the misalignment between the object and the hydrostat, suggesting that the model curve should be shifted along the x-axis. This adjustment would improve the comparability between the initial increase in the normalized figures of the model and the data.

4.3. Object Wetting

Expanding on the previous point regarding the wettage difference due to distance d_{tw}, figure 12c demonstrates that when the object has a downward curvature (a negative dR_o/dx), the hydrostat also struggles to follow the object's shape. Instead, it extends straight out creating a larger distance d_{tw}. After additional actuation the hydrostat does conform to the object's shape in a rapid manner, as depicted in figure12d.

At this stage, the gravitational force exerted by the water in the tip of the hydrostat is insufficient to cause it to curve downward. With further actuation, enough water accumulates in the tip to overcome the stiffness of the silicone. This stiffness effect is largely dependent on the membrane's thickness, becoming more pronounced with greater thickness. Additionally, when gripping objects with larger radii, even less water is present in the tip of the hydrostat, exacerbating this issue.

Since the model assumes perfect wetting of the object, deviations between the measured data and the model predictions are expected. The descending curves in the sphere push tests illustrate this discrepancy. As shown in figure 12c, there is no axial force on the back of the sphere, resulting in a higher disturbance force.

When there is a significant overhang and a pull test is initiated, the overhang starts to shape around the object, but a not-

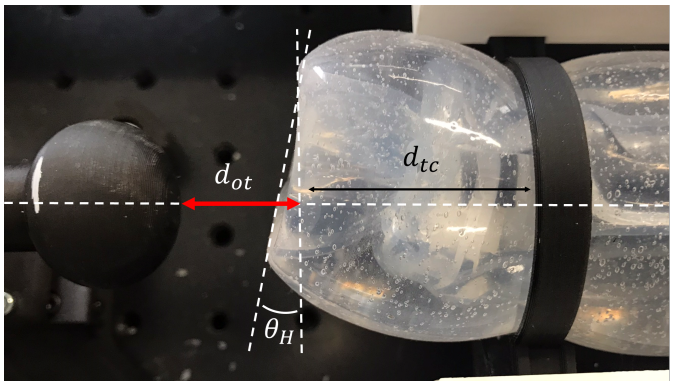

(a) Distance between the test object and hydrostat d_{ot} and distance between the hydrostat's tip an the carrier d_{tc}, exaggerated for clarity.

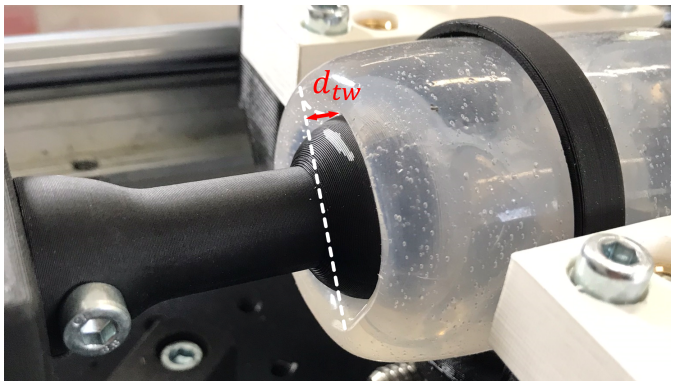

(b) Distance between the hydrostat's tip and the beginning of the object's wetting d_{tw}, attributed to the curvature of the tip.

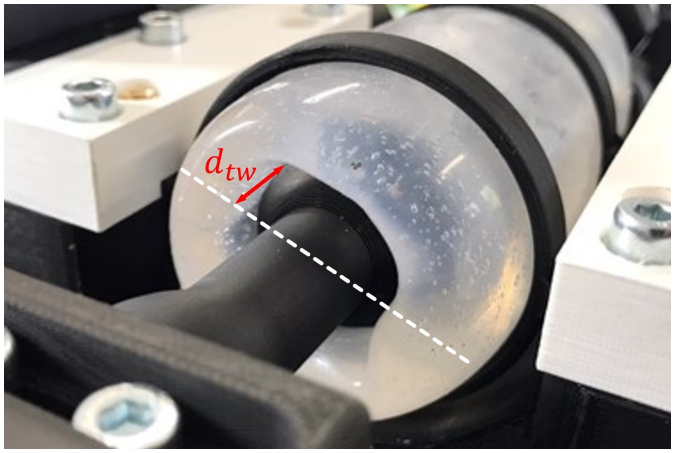

(c) Hydrostat struggles to conform to the downward curvature of the sphere, increasing the distance d_{tw}.

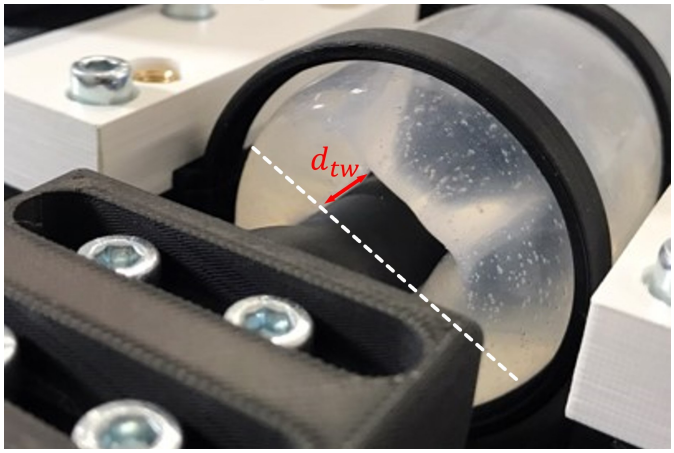

(d) Illustrating that after further actuation, the hydrostat successfully conforms to the shape of the object, reducing the distance d_{tw} and ensuring proper wetting.

Figure 12: The distance offset identified during model tuning is attributed to two main factors: the misalignment due to the curving of the hydrostat causing a gap between the object and the tip of the hydrostat d_{ot}, and the curved tip of the hydrostat affecting the distance between the hydrostat's tip and beginning of the object's wetting d_{tw}. Additionally, the hydrostat struggles to conform to objects with a large downward curvature, further increasing d_{tw}. After further actuation, the hydrostat does conform to the shape.

able visual difference remains between the actuated and true swallow distances.

With more intricate objects that have high values of dR_o/dx, the hydrostat will likely struggle to conform to the object's shape, potentially failing to make full contact in some areas. This imperfect wetting will significantly impact the magnitude of the holding force, making accurate model predictions difficult.

4.4. Axial Strain

The axial strain of the hydrostat is not accounted for. In reality, the hydrostat becomes slightly shorter when it expands over an object, further decreasing the true swallow distance. This effect is considered to be small but becomes more noticeable when gripping larger objects.

4.5. Investigating the High Tuning Parameter

The unexpectedly high tuning parameter ($c = 1.45$) raises questions, particularly considering that all parameters are realistically expected to only deviate within roughly a 20% range of their initial values. Additional tests were conducted using a cylinder with a 150% increased diameter. This test piece, printed with a different 3D printer under less optimal settings, had a rougher surface compared to the smooth surfaces of the other test pieces.

Unexpectedly, this larger test piece exhibited a much lower friction force than anticipated, roughly a factor of 2 lower than estimated. While a minor change in the friction coefficient could account for some difference, it likely does not explain the entire discrepancy.

During tests with the original smooth test pieces, a vacuum was observed behind the test piece during pull tests. However, this vacuum was not observed with the larger, rougher test piece. This difference can be attributed to the hydrostat being closed off with a tie wrap and not being fully hollow, creating a closed volume behind the object within the hydrostat.

This suggests that additional forces, such as a vacuum force, may be acting on the smooth test pieces. However, this force than would also have to scale linearly with the swallow distance. If it would be a constant force, the curve in figure 7 would shift downward by a constant amount, resulting in an unrealistically large distance offset. However, the idea that this

force would scale linearly seems questionable.

If additional forces are indeed present, the friction force has been overestimated, and consequently, so has the tuning parameter. A decrease in this parameter would result in the model better approximating the disturbance force.

4.6. Limitations of the Model

The model seems to operate under most conditions. However when $max(R_o(x)) > R_i$, the inner membrane of the hydrostat begins to stretch, introducing additional forces that are not considered in the model. Consequently, at this limit, the model becomes invalid.

4.7. Dimensional Limits

During the manufacturing of the hydrostat, several challenges were encountered, highlighting limitations in the manufacturing process.

There seems to exist a critical range of pressures crucial for the hydrostat's functionality. Although precise pressure measurements were not taken, pressure was inferred through the metric R_H/R_i. At low pressures, the hydrostat sags unto itself, buckles and is not operational. As pressure increases, the hydrostat's opening narrows and distorts, making it increasingly difficult to grasp objects. Although the exact pressure range is unknown, it suggests the existence of an optimal range for the pressure-to-elasticity ratio P/E.

As the initial radius Ri increases significantly, so does the water volume within the hydrostat, which increases the influence of the the gravitational force. For small membrane thicknesses, this will potentially result in a 'belly' forming at the bottom of the gripper, which seems undesirable. This indicates that there is a probably an upper limit to R_i/t_i.

When the hydrostat's length L_H is too small, it cannot effectively grip objects. If L_H is too large, the hydrostat folds and buckles during operation, becoming non-functional. The minimum length appears to be the desired swallow length plus any misalignment length, which in practice is likely around 1.5 times the desired swallow length. The maximum length is not precisely known, but it is depended on both the membrane thickness and the initial hydrostat radius. Based on personal experience, a hydrostat length exceeding 200 *mm* tends to cause issues.

5. Conclusion

In summary, this study successfully extends the existing parametric model of the holding force for a toroidal hydrostat gripper, as developed by Root et al.(8), by incorporating the axial disturbance force during grasping and adjusting the model to accommodate variable radii. Through validation using an experimental setup, parameter uncertainties are resolved by measuring the holding forces during pull tests on an object with a constant radius and at a constant hydrostatic pressure. This demonstrates the expected linear relationship between the friction force and the swallow distance excellently, validating the work by Root et al. (8).

A discrepancy is discovered between the actuated swallow distance and the true swallow distance. This is caused by the hydrostat's tip curvature and its struggle to conform to the object's shape when curving downward, introducing a distance d_{tw} between the hydrostat's tip and the object's initial wetting point.

Pull tests on spherical objects show that the friction force is well approximated by the model, with only a maximum deviation of 15% at the maximum swallow distance. Push tests conducted on spherical and conical-shaped objects reveal that the model overestimates the disturbance force by a factor of 2.5-3. However when both curves are normalized against their maximum values, the shape of both curves show good resemblance. The end of the data curve shows some irregularities, attributed to d_{tw}.

A difference in peak disturbance force is discovered due to the distance between the object and the actuation rod d_{or}. The disturbance force increases by up to 25% when d_{or} is decreased from 50 to 10 *mm*. This increase is attributed to the piece of silicone between the object and the actuation rod, which behaves more like a spring than a rigid body, with a spring constant that increases as d_{or} decreases.

Dimensional limits are identified. There appears to be an optimal range for the pressure-to-elasticity ratio P/E for the hydrostat to function properly. Additionally, there seems to be an upper limit to the ratio of the initial hydrostat radius to the membrane thickness R_i/t_i, to prevent an undesirable 'belly' formation at the bottom of the gripper. The minimum hydrostat length appears to be 1.5 times the desired swallow length.

A high tuning parameter of $c = 1.45$ is discovered during model tuning, which suggests that other than the hydrostatic forces, another force may act on the object. A vacuum was observed during the pulling tests, which occurred only on smooth-surfaced objects rather than on slightly textured surfaces. This implies a potential additional vacuum force. If this additional force is present, the friction force would decrease, reducing the tuning parameter and the magnitude of the predicted disturbance force, thereby improving the model's estimation of the disturbance force.

Future research should focus on investigating the potential vacuum force that may be influencing the results, examining the impact of d_{or} on the disturbance force, and exploring the dimensional limits, so an optimal operational hydrostat gripper can be designed.

6. Supplementary information

Supplementary information on the mathematical derivation, Matlab implementation, manufacturing process, detailed explanation of the test setup and testing procedures, additional results, hand-held gripper models, and the manufacturing of textured hydrostats can be found in the appendices below.

References

[1] L. Birglen and T. Schlicht, "A statistical review of industrial robotic grippers," vol. 49, pp. 88–97.

[2] T. K. Lien, "7 - gripper technologies for food industry robots," in *Robotics and Automation in the Food Industry* (D. G. Caldwell, ed.), Woodhead Publishing Series in Food Science, Technology and Nutrition, pp. 143–170, Woodhead Publishing.

[3] J. Shintake, V. Cacucciolo, D. Floreano, and H. Shea, "Soft robotic grippers," vol. 30, no. 29, p. 1707035. _eprint: https://onlinelibrary.wiley.com/doi/pdf/10.1002/adma.201707035.

[4] Z. Wang, K. Or, and S. Hirai, "A dual-mode soft gripper for food packaging," vol. 125, p. 103427.

[5] S. Zaidi, M. Maselli, C. Laschi, and M. Cianchetti, "Actuation technologies for soft robot grippers and manipulators: A review," vol. 2, no. 3, pp. 355–369.

[6] Y. A. AboZaid, M. T. Aboelrayat, I. S. Fahim, and A. G. Radwan, "Soft robotic grippers: A review on technologies, materials, and applications," vol. 372, p. 115380.

[7] Y. Liu, J. Hou, C. Li, and X. Wang, "Intelligent soft robotic grippers for agricultural and food product handling: A brief review with a focus on design and control," vol. 5, no. 12, p. 2300233. _eprint: https://onlinelibrary.wiley.com/doi/pdf/10.1002/aisy.202300233.

[8] S. E. Root, D. J. Preston, G. O. Feifke, H. Wallace, R. M. Alcoran, M. P. Nemitz, J. A. Tracz, and G. M. Whitesides, "Bio-inspired design of soft mechanisms using a toroidal hydrostat," vol. 2, no. 9, p. 100572.

[9] D. Sui, Y. Zhu, S. Zhao, T. Wang, S. K. Agrawal, H. Zhang, and J. Zhao, "A bioinspired soft swallowing gripper for universal adaptable grasping," vol. 9, no. 1, pp. 36–56. Publisher: Mary Ann Liebert, Inc., publishers.

[10] A. Kaleem, S. Hussain, M. Aqib, M. J. M. Cheema, S. R. Saleem, and U. Farooq, "Development challenges of fruit-harvesting robotic arms: A critical review," vol. 5, no. 4, pp. 2216–2237. Number: 4 Publisher: Multidisciplinary Digital Publishing Institute.

Contents

Appendix A. Derivation of the parametric Model

This appendix section builds upon the formulas provided by Root et al.(1), extending them to derive the holding and disturbance forces of a hydrostat gripper during gripping and grasping.

The model's derivation begins by considering the normal force F_N exerted by the hydrostat on an object. This force is a product of the hydrostatic pressure P and the object's surface area A_o:

$$F_N = PA_o \tag{A.1}$$

The hydrostatic pressure is generated due to the stretching of the hydrostat's outer membrane with radius R_H and thickness t_i. This pressure is related to the circumferential stress σ in the membrane through the thin-walled hoop formula:

$$P = \frac{\sigma t_H}{R_H} \tag{A.2}$$

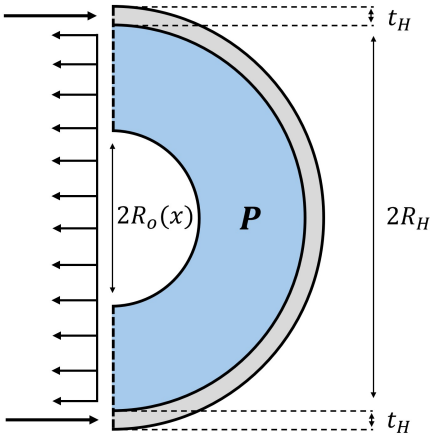

Figure A.13: Free Body Diagram of a cross-section of the hydrostat. The grey section represents the silicone membrane of the hydrostat, while the blue section represents the water contained within the hydrostat.

The stress in the membrane is related to the circumferential strain ε and the Young's modulus E via Hooke's law:

$$\sigma = E\varepsilon \tag{A.3}$$

To account for the nonlinear stress-strain relationship of the silicone, the Young's modulus is not treated as a constant. Instead, it is represented as a function of the strain through a sixth-order polynomial determined through tensile testing described in Appendix F.

$$\sigma = E(\varepsilon)\,\varepsilon \tag{A.4}$$

The circumferential strain is defined as the ratio of the change in the hydrostat's radius to its initial non-pressurized radius R_i:

$$\varepsilon = \frac{R_H - R_i}{R_i} \tag{A.5}$$

Assuming a Poisson's ratio of $\nu = 0.5$, the relationship between the initial membrane thickness and the hydrostat's radius can be described by:

$$\frac{R_i}{R_H} = \frac{t_H}{t_i} \tag{A.6}$$

The hydrostat's radius can be determined by the conservation of volume. The total volume V_H is the sum of the initial pressurized hydrostat volume V_{H0}, the volume of the actuation rod V_r, and the volume of the object V_o:

$$V_H = V_{H0} + V_r + V_o \tag{A.7}$$

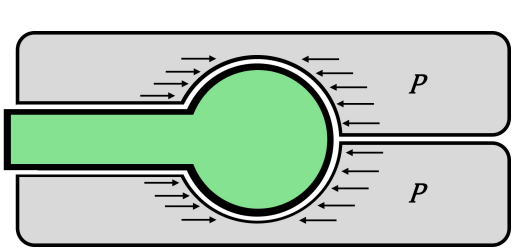

(a) Forces in the axial direction

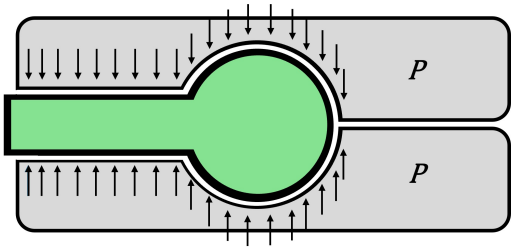

(b) Forces in the radial direction

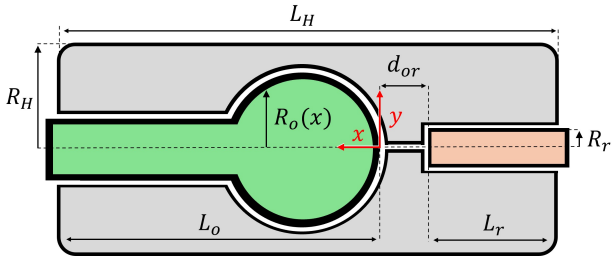

(c) Depiction of the object and the rod in the test setup

Figure A.14: Schematic cross-sectional view of the hydrostat, illustrating the hydrostat in grey, the object in green and the actuation rod in orange

V_H, V_{H0}, and V_r can each be expressed as cylinders with constant radii, while V_o can be expressed as a cylinder with a variable radius:

$$V_n = \pi R_n^2 L_n \quad \text{for} \quad n \in \{H, H_0, r\} \tag{A.8}$$

$$V_o = \pi \int_0^{L_o} (R_o(x))^2 \, dx \tag{A.9}$$

Assuming the pressure is uniformly distributed throughout the hydrostat, R_H can be expressed as:

$$R_H = \sqrt{\frac{V_{H0} + V_r + V_o}{L_H \, \pi}} \tag{A.10}$$

By combining equations A.1 to A.6, the normal force exerted on the object can be formulated as follows:

$$F_N = A_o E(\varepsilon) R_i t_i \left(\frac{1}{R_H R_i} - \frac{1}{R_H^2} \right) \tag{A.11}$$

The normal forces are then projected onto two different areas: the radial area A_{oR} and axial area A_{oA}, both as a function of the variable radius $R_o(x)$ at $x = L_o$:

$$A_{oR} = 2\pi \int_0^{L_o} R_o(x) \, dx \tag{A.12}$$

$$A_{oA} = \pi R_o^2(L_o) \tag{A.13}$$

By substituting these area equations into the normal force equation, we derive two separate force equations: force in the radial direction F_R, and the force in the axial direction F_A.

$$F_R = A_{oR} E(\varepsilon) R_i t_i \left(\frac{1}{R_H R_i} - \frac{1}{R_H^2} \right) \tag{A.14}$$

$$F_A = A_{oA} E(\varepsilon) R_i t_i \left(\frac{1}{R_H R_i} - \frac{1}{R_H^2} \right) \tag{A.15}$$

Finally, the holding force and the axial disturbance force during grasping can be expressed as:

$$F_{Hold} = \mu F_R - F_A \tag{A.16}$$

$$F_{Dist} = F_A \tag{A.17}$$

Appendix B. Matlab Implementation

Appendix B.1. Numerical Implementation

MATLAB is used to calculate the holding and disturbance forces using a numerical approach. To facilitate this, all formulas dependent on the swallow distance x must be converted from continuous to discrete equations. Since only the radius of the object is a function of x, the area formulas need to be adjusted accordingly. The area functions are transformed into discrete equations, and for the radial area, the numerical trapezoidal rule is applied (2):

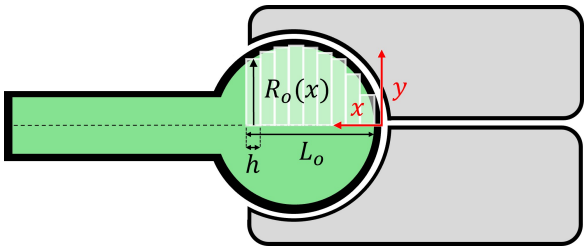

Figure B.15: Numerical interpretation of the object's area's.

$$A_{o_{Radial}}[n] = 2\pi h\left(\frac{1}{2}R_o(0) + \sum_{i=1}^{n-1} R_o(ih) + \frac{1}{2}R_o(l_o)\right) \tag{B.1}$$

$$A_{o_{\text{Axial}}}[n] = \pi R_o^2(nh) \tag{B.2}$$

A condensed version of the MATLAB code is presented below. Here is an explanation of its structure: the code is divided into three parts: Initialization, Numerical Integration, and Finalization. Additionally, some MATLAB functions need to be created.

Initialization The material and dimensional constants are loaded from an additional file, and the numerical variables are set for the swallow distance x_G and the number of steps n. The distance offset obtained from the optimization is applied. The object's radius is obtained via the function `GetShapeRadius`.

Numerical Integration First, the required matrices are pre-allocated. Then, in a for-loop, the hydrostat radius, hydrostatic pressure, and radial and axial areas are calculated for each step n using the functions `RH_func` and `Pressure_func`.

Finalization The product of the pressure and areas is taken, the radial and axial forces are determined, and the disturbance and holding forces are calculated. Additionally, an x-vector holds the distance. This results in three vectors: Disturbance Force, Holding Force, and Distance.

`GetShapeRadius`. Create a function file which outputs the object's radius from $x = 0 : x_G$ in n intervals.

`Pressure_func`. Using the symbolic toolbox in Matlab, write out all the variables and equations A.2-A.6. Create a strain variable x and load in the non-linear function of the Young's modulus as a function of x and use `eval` to make it a function of the dimensional constants. Lastly, the tuning parameter is added. Now use the function `matlabFunction` to obtain the function file.

`RH_func`. Create a function file that outputs the hydrostat radius using the following inputs: object radius, step, step size, and material and dimensional constants. Use equations A.7-A.10 to determine RH.

Main Script

```
%% Initialize
run Constants.m                 % obtain Material and Dimesional
  constants
x_G = 50;                       % Determine Gripping distance
x_offset = 0;                   % Distance offset
x_G_o = x_G - x_offset;         % offset distance
n = 100;                        % set the amount of steps
h = x_G_o/n;                    % stepsize
Ro_n = GetShapeRadius(x_G_o,n); % obtain object's Radius devided into
  n steps
c_opt = 1;                      % tuning parameter

%% Numerical Integration
% Pre-Allocate Pressure and Radial and Axial Area Matrices
RH_n = zeros(n-2,1);  P_n = RH_n;   AR_n = RH_n;      AA_n = RH_n;

for i = 1:n-2
    RH_n(i) = RH_func(Ro_n(1:i+1), n, h, C);      % Determine RH as a
      function of Ro and the Constants
    P_n(i)  = Pressure_func(RH_n,C,c_opt);  % Determine the Pressure

    AR_n(i) = 2*pi*h* (0.5*Ro_n(1) + sum(R0_n(2:i+1)) + 0.5*Ro_n(end))
      ; % Determine
    AA_n(i) = 2*pi* Ro_n(i+1)^2;
end

%% Finalize
FR_n    = P_n.*AR_n;
FA_n    = P_n.*AA_n;

F_ROL   = FA_n;
F_HOLD  = FR_n * mu - FA_n;
```

Pressure_func

```
syms RH Ri ti c_opt
x = ((RH-Ri)/Ri);           % Strain
[E,~] = GetYoungsM();       % 6th order polynomial from measurements
  as a function of the strain x

t = (Ri/RH)*ti;             % Membrane thickness
P = (E*x*t)/(RH);           % Hydrostatic Presure

P = c_opt*P;                % For the tuning parameter
matlabFunction(P,'File','Pressure_Func');
```

RH_func

```
function RH = RH_func(Ro_n, n, h, C)
RH0 = C(1);      % Initial hydrostat radius
Rr  = C(2);      % radius actuation rod
Lr0 = C(3);      % initial length actuation rod
LH  = C(4);      % Length hydrostat

Lr = Lr0 - n*h; % Determine actual length actuation rod

% Determine Volumes
VH0 = pi * RH0^2 * LH;
Vo  = sum(h * pi * Ro_n.^2);
Vr = pi * Rr^2 * Lr;
Vtot = VH0 + Vo + Vr;

% Determine RH
RH = sqrt(Vtot/(pi*LH));
end
```

Appendix B.2. Model fitting algorithm

The model's dimensional and material parameters E, t_i, R_i, R_H and μ cannot be determined with high accuracy. To address these uncertainties, the model is fitted against measured data. Each parameter is assigned a tuning parameter C_n. These constants can be approximated into a single constant C in the friction force formula $F_f = \mu F_R$:

$$C_1 E, \quad C_2 t_i, \quad C_3 R_i, \quad C_4 R_H, \quad C_5 \mu \tag{B.3}$$

$$F_f = C_5 \mu A_{oR} C_1 E(\varepsilon) C_3 R_i C_2 t_i \left(\frac{1}{C_4 R_H C_3 R_i} - \frac{1}{C_4^2 R_H^2} \right) \tag{B.4}$$

$$F_f \approx C \mu A_{oR} E(\varepsilon) R_i t_i \left(\frac{1}{R_H R_i} - \frac{1}{R_H^2} \right) \tag{B.5}$$

The parameters μ, R_i and t_i are constants, and when R_H is also constant, $E(\varepsilon)$ remains constant according to equation A.5. Under these conditions, F_f scales only with $C\ A_{oR}$. Additionally, if the object is cylindrical, where $R_o(x) = R_o$, F_f scales linearly with $C\ L_o$.

$$A_{oR} = 2\pi \int_0^{L_o} R_o(x)\, dx = 2\pi R_o L_o \tag{B.6}$$

$$F \propto C L_o \tag{B.7}$$

By utilizing a optimization algorithm and fitting the model to the measured data of the friction force on a cylinder, the constant C can be determined. The MATLAB code is presented below and is divided into three parts: Data Analysis, Linear Function, and Optimization. Additionally, a cost function needs to be written for the optimization algorithm.

Data Analysis Load the data and determine the number of different swallow distance measurements taken, as well as the number of measurements per swallow distance. Obtain the force vector for each measurement, then extract the initial and maximum values. The maximum value represents the maximum holding force. According to equation A.16, at the initiation of the pull test, $F_R = 0$, indicating that the initial force is F_A. Then the friction force is determined.

Linear Function The mean of the different measurements per swallow distance is calculated, and a 1st order function is fitted through the mean data points using `polyfit`. The distance offset is determined by the point where this function crosses the x-axis.

Optimization The function `fmincon` is used for optimization. Initialize the starting point, and set the upper and lower bounds for the tuning parameter. The optimization process is then performed using the function `costfunction`.

`costfunction`. Create a costfunction that outputs the cost of a minimization function as a function of the tuning parameter (3). The goal is to minimize the difference between the data and the model. Determine the friction force for the values in the `distance` vector for both the data and the model, subtracting the earlier obtained distance offset from the model's distance. Normalize the forces against the data so each data point has equal weight. Subtract the model's force from the data's force, sum these differences, and take the absolute value to turn it into a minimization function.

Main Optimization Script

```
%% Data analysis
% Load in data from text files
Pull_data = {'24 04 26 10 39 48 R16t14Dummy00_40_Pull_1.txt',...
             '24 04 26 10 41 36 R16t14Dummy00_40_Pull_2.txt',...
             '24 04 26 10 43 18 R16t14Dummy00_40_Pull_3.txt',...
             '24 04 26 10 44 59 R16t14Dummy00_30_Pull_1.txt',...
             '24 04 26 10 46 17 R16t14Dummy00_30_Pull_2.txt',...
             '24 04 26 10 47 39 R16t14Dummy00_30_Pull_3.txt',...
             '24 04 26 10 49 01 R16t14Dummy00_20_Pull_1.txt',...
             '24 04 26 10 50 06 R16t14Dummy00_20_Pull_2.txt',...
             '24 04 26 10 51 06 R16t14Dummy00_20_Pull_3.txt'};

numFiles = length(Pull_data);      % Determine length Pull_data
distances = [40 30 20];            % distances measured
n_distance    = length(distances); % number of distances
n_measurement = 3;                 % No measurements per distance

% Pre-allocate Matrices
forceHigh = zeros(1, numFiles); forceZero = zeros(1, numFiles);
for i = 1:numFiles
    data = load(Pull_data{i});                  % Load data from file
    forceColumn = -1*(data(:, 4)); % Get force
    forceHigh(i) = max(forceColumn);            % Get maximum force
    forceZero(i) = forceColumn(1);              % Get initial force
end

% Determine friction force
force_friction = forceHigh - forceZero;

% Get mean friction force per distance
k = 1;
for i=0:n_measurement:numFiles - n_measurement
        force_friction_mean(k) = mean(force_friction(i+1:i+
          n_measurement));
        k = k+1;
end

%% Linear function
% Create linear function of the data
syms x

trend = polyfit(distances,force_friction_mean,1);
trendSym = sym(trend);
trendSym = poly2sym(trendSym, x);
ftrend =  matlabFunction(trendSym,'File','fTrend');

% Determine and display distance offset
xval0 = eval(solve(trendSym == 0));
disp(xval0(1))

%%
x0 = 1;
```

```
lb = 0;
ub = 10;
options = optimoptions('fmincon','Display','iter');

[x Fval] = fmincon(@costfunction,x0,[],[],[],[],lb,ub,[],options)
```

Cost Function

```
function cost = costfunction(x)

run Constants.m
c_opt = x(1);                % Determine tuning parameter

% Pre-allocate
Fc = zeros(size(d));

% Get 'measured data' from linear function
data = fTrend(distance);

for i=1:length(distance)
    P = Pressure_Func(RH,C,c_opt);
    AoR = 2*pi*Ro*(distance(i)-distance_offset);
    Fc(i) = mu*AoR*P;
end

FcNorm = Fc./data;
cost = abs(sum(FcNorm) - sum(data./data));
end
```

Appendix C. Manufacturing

The hydrostats are essentially sleeves that are folded unto themselves, filled with water, and sealed off. Manufacturing of the hydrostat can therefore be seen as 2 seperate acts: sleeve manufacturing and hydrostat assembly.

Appendix C.1. Sleeve Manufacturing

The manufacturing process of the sleeves involved investigating multiple manufacturing techniques for various materials. Important for these sleeves are that they can be manufactured with different lengths, radii, and thicknesses, while maintaining uniformity in thickness. Additionally the material is not to be plastically deformed when stretched within its operational range, ideally elastomers are great for this. Finally, to achieve a high holding force, the friction coefficient should be sufficiently high. Three materials/manufacturing methods were considered: silicone, latex, and LDPE film.

Appendix C.1.1. Materials and Manufacturing Processes

Silicone Silicone is an elastomer widely utilized in soft robotics because of its high elasticity and capacity for significant strain within its elastic deformation range. It demonstrates excellent durability, enduring repeated cycles of stretching and compression without significant wear or performance loss.

Several manufacturing methods for silicone were identified: extrusion, injection molding, liquid injection molding, compression molding, calendering, and transfer molding (4). Additionally, Root et al.(1) proposed a method involving brushing silicone onto a rotating pipe.

Among these methods, extrusion and brushing are particularly well-suited for creating long sleeves with varying radii and thicknesses.

Extrusion. This technique is designed for producing items with uniform cross-sectional shapes, such as sleeves. Silicone is forced through a heated extruder to form the desired shape and then cooled. Extrusion is ideal for producing sleeves due to its short curing times, high production capacity, and precision in maintaining uniform thickness. However, it involves high operational costs.

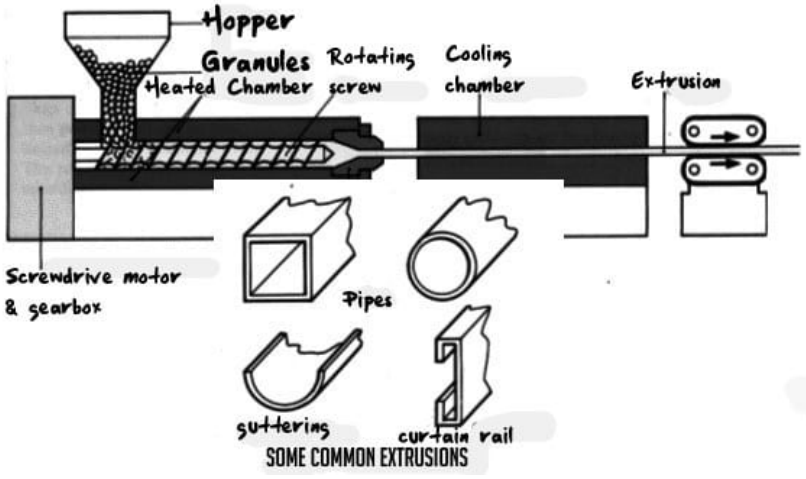

Figure C.16: Extrusion manufacturing method (4): Silicone is forced through a heated extruder to form the desired shape and then cooled.

Brushing Method. This method uses silicone that hardens at room temperature, applied manually to a rotating pipe. The rotation ensures even distribution of the silicone across the pipe's radius and prevents dripping as it hardens over approximately 12 hours. While this method has lower operational costs, the uniformity of the thickness is less precise due to manual application.

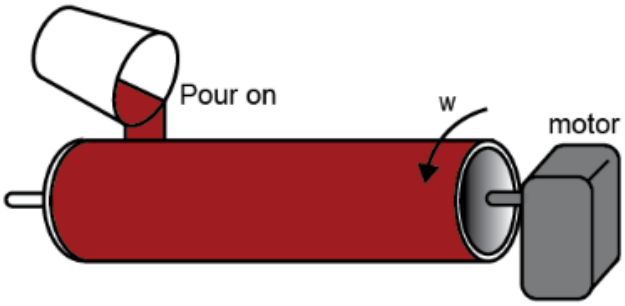

Figure C.17: Brushing manufacturing method (1): Liquid silicone is applied to a rotating pipe. The rotation ensures uniform thickness and prevents dripping.

The extrusion method allows for more precise control over the sleeve's thickness compared to the brushing method, making it preferable for final gripper designs. However, for prototyping purposes, the brushing method is favored due to its simplicity and low cost, making it an effective in-house manufacturing solution.

Latex Latex is also an elastomer, similar to silicone. It exhibits high durability and is highly resistant to tears and punctures, making it ideal for applications requiring water tightness.

The primary manufacturing method for latex is dipping. In this process, a metal mold is preheated to 80°C and then dipped into a liquid latex bath. Over the course of about a minute, the liquid latex begins to solidify on the mold's surface. Once the desired thickness is achieved, the mold is slowly removed from the bath at a consistent speed to ensure a smooth texture. The sleeve is then cured either by heating it in an oven at 70-80°C for 20 minutes or by allowing it to hang at room temperature for 12-24 hours. After curing, the sleeves are dusted with talc powder to prevent them from sticking together. A video explaining this method can be found here.

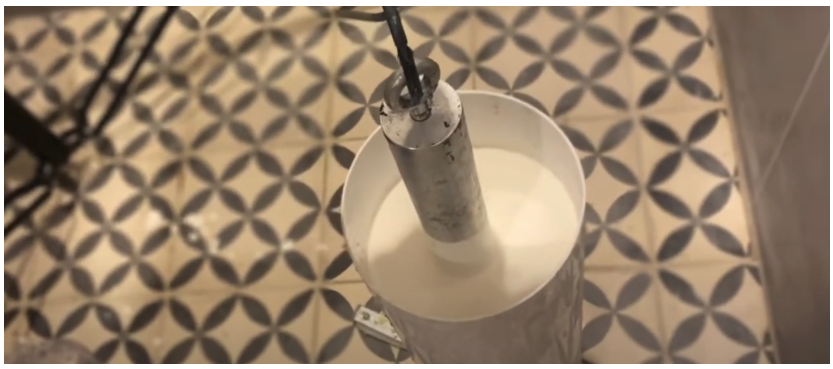

Figure C.18: Latex dipping method (5): A heated rod is dipped in liquid latex. The latex solidifies against the rod and is pulled out of the bath at a constant speed to ensure a smooth finish.

LDPE An honorable mention is the use of LDPE film. Although LDPE is not an elastomer and has roughly 100 times the Young's modulus of silicone, Berthet-Rayne et al.(6) utilized this film to create long sleeves for an extruding pressurized sleeve. However, for LDPE to be useful in gripping applications, The forces need to be comparable to those produced by latex or silicone. This would require the thickness to be approximately 100 times thinner than 1mm, which is not feasible. Despite this limitation, for applications requiring much higher forces and less expansion, this affordable and easy-to-use method may be a viable option.

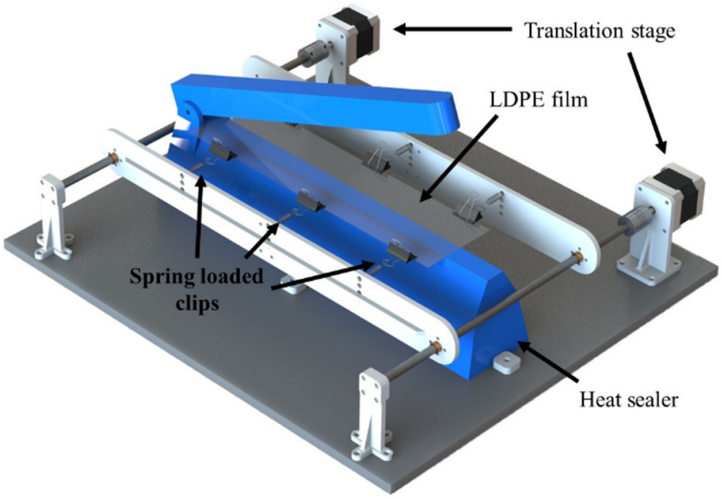

Figure C.19: Manufacturing device of LDPE film (6): The film is folded, and the ends are heat-sealed together.

Choosing the Silicone Brushing Method The silicone brushing method was chosen over the latex dipping method for several reasons. Both options appeared viable for in-house prototyping, but the silicone method required significantly less material to initiate, with most of the necessary items being readily accessible. Additionally, the silicone method provided greater control over thickness, as the silicone's weight is measured beforehand. In contrast, the thickness in the latex dipping method depends on dipping time, with ambient temperature and the mold's temperature being potential significant factors. Furthermore, the latex method necessitated a slow withdrawal from the bath to avoid drips on the sleeve, potentially causing an undesirable thickness gradient along the sleeve's length. At the time, gluing seemed to be the only option for eventually sealing the hydrostat. Root et al. (1) demonstrated that this was feasible using a specific silicone glue for the silicone method. The effectiveness of gluing for latex was uncertain, giving the silicone brushing method the final edge.

Selection of Silicone Numerous types and brands of silicone available on the market, each tailored for specific applications. For this particular application, a silicone that cures at room temperature is required. Additionally, a significant working time is required to ensure it doesn't begin to solidify prematurely when applied to the rotating pipe. Root et al. (1) used SMOOTH-ON SORTA-CLEAR 12 silicone for their prototypes. Given its proven effectiveness and for the sake of repeatability, SORTA-CLEAR 12 was selected.

According to SMOOTH-ON, SORTA-CLEAR 12 silicone "cures at room temperature with negligible shrinkage and features high tensile and tear strength" (7). This silicone can stretch up to 590% of its original length before tearing. It has a pot life of 40 minutes, providing enough time for mixing and application, and a curing time of 12 hours. The Shore hardness of SORTA-CLEAR 12 is 12A, indicating the material's resistance to indentation. Although formulas exist to convert Shore hardness to Young's modulus, the relationship is not direct (8). Additionally, SMOOTH-ON provides a 100% modulus, which represents the stress required for 100% elongation. In linear materials, this would be equivalent to Young's modulus, but due to the nonlinear stress/strain relationship, this is not the case. Therefore, during testing, measurements were conducted to determine the material's stress/strain relationship, detailed in Appendix F.

Appendix C.1.2. Sleeve Manufacturing Setup

A small sleeve manufacturing rig was developed, featuring a 100 rpm, 12V-DC motor rotating a PVC pipe, all mounted on a wooden frame with 3D-printed brackets. The motor is wired in series with a potentiometer, allowing for easy adjustment of the motor's speed on the fly.

The 32mm diameter, 400mm long PVC pipe is connected to the motor using an aluminum rod. This rod is secured to the PVC pipe with 3D-printed parts that are press-fitted into both the pipe and the rod. A small 3D-printed insert, press-fitted onto the shaft of the DC motor, fits into the aluminum rod. The connection is then

secured with a piece of duct tape, allowing for easy detachment when the sleeve needs to be removed from the PVC pipe.

(a) Exploded view of the manufacturing rig consisting of a PVC pipe, an aluminum rod, 3D-printed mounting brackets and inserts, and a 12V-DC motor.

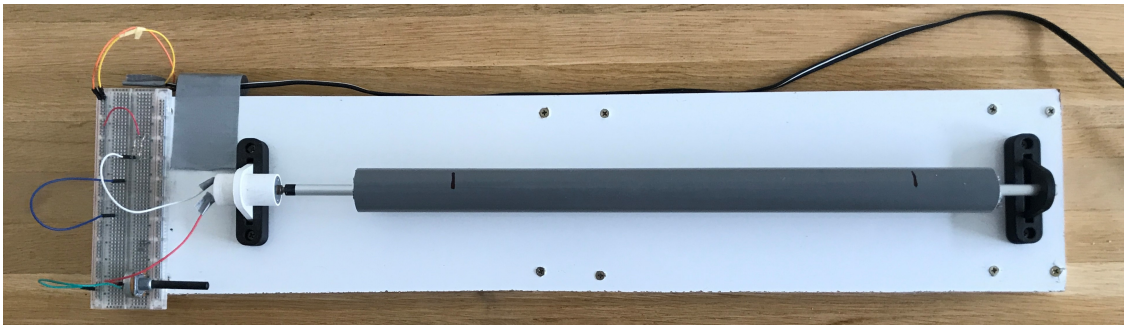

(b) Photograph of the physical manufacturing rig, featuring a breadboard and potentiometer.

Figure C.20: Exploded view and photograph of the manufacturing rig.

Appendix C.1.3. Sleeve Manufacturing Steps

For the manufacturing process, the following items are needed:

- Manufacturing rig
- SORTA-CLEAR 12A liquid silicone
- Scale
- Small stirring rod
- Plastic stirring cups
- Duvet vacuum storage bags or another vacuum device
- Silicone spatula

Next, determine how much silicone you need. For a $32mm$ diameter, $400mm$ sleeve, $24g$ each of part A and part B of SORTA-CLEAR 12A silicone is used to achieve a thickness of $0.6mm$, which approximates to roughly $0.06g/cm^2$. Note that this is not exact, as there will always be some silicone residue left in the cup.

The advisable maximum layer thickness is $0.6mm$. When a thicker sleeve is required, it should be built up in multiple layers. It is not recommended to apply a layer thicker than $0.6mm$, as this can result in silicone pimples on the sleeve as can be seen in figure C.21. The outer layer will start to solidify earlier than the inner layer, causing the outer layer to be displaced due to centrifugal force. Furthermore, the minimum layer thickness is roughly $0.3mm$. Thinner thicknesses are difficult to achieve, as the viscous silicone cannot be spread evenly across the surface, resulting in gaps.

Figure C.21: Silicone droplets forming on the sleeve due to excessive silicone use.

The manufacturing process can be described in the follow steps:

1. As per the manufacturer's instructions, stir SORTA-CLEAR parts A and B rigorously. Add the desired amount of silicone to the plastic cup in a 1:1 weight ratio and mix thoroughly.

2. Stirring introduces bubbles into the silicone, which can cause the sleeve to tear easily, especially in single-layer sleeves. To prevent this, the manufacturer recommends applying a vacuum degas of at least 1 bar. An accessible method is using vacuum bags designed for storing duvets, which can be used with a vacuum cleaner. Vacuum the silicone for 1 minute to remove the majority of the bubbles. Firmly tapping the cup on the floor will help pop the remaining bubbles that rise to the surface.

3. Turn on the motor of the manufacturing rig and set it to its highest speed, which for me was approximately 100 rpm. This high speed helps spread the silicone evenly across the pipe. Begin by pouring the silicone onto the rotating PVC pipe (depicted in figure C.22), making sure to distribute it evenly along the length of the pipe to ensure a uniform thickness. Once all the silicone is applied, use a silicone spatula to further distribute it. Hold the spatula flat against the pipe and slowly move it along the length, ensuring there are no dry spots. If any air bubbles surface, pop them with the spatula; the rotation of the pipe will help smooth out the small indentations left by the popped bubbles.

4. Once satisfied with the uniformity of the silicone, reduce the RPM to the lowest setting. This slow rotation helps prevent the silicone from dripping while ensuring it remains evenly spread. Maintaining a low RPM is crucial, as higher speeds can still cause pimples to form on the silicone surface.

5. Allow the silicone to cure for 3 hours. If additional coats are needed, repeat the steps above. If no additional coats are required, the motor can be turned off, but let the silicone dry for an additional 12 hours to ensure it is fully cured.

6. Once cured, the silicone sleeve can be rolled off the pipe. Trim the thinner edges with a knife for a clean finish.

(a) Pouring liquid silicone onto the PVC pipe at a constant speed.

(b) Spreading the silicone evenly across the pipe with a silicone spatula to ensure uniform thickness.

(c) Final cured silicone sleeve on the PVC pipe.

Figure C.22: Manufacturing steps for creating a silicone sleeve.

Appendix C.1.4. Sleeve Thickness Uniformity

24 grams each of parts A and B were used to fabricate a sleeve with a diameter of 32*mm* and a length of 400*mm*. The middle section was cut out, and thickness measurements were taken every 20 mm using a caliper, as depicted in figure C.23a. Each row was cut off while measuring to ensure accurate readings for each spot. Figure C.23b shows the boxplot of those measurements. Most measurements fall within the range of 0.6-0.8*mm*, with the greatest variation in thickness occurring lengthwise rather than radially.

While initially it was assumed that uniform thickness was crucial for good results, this relatively non-uniform hydrostat performed perfectly. When pressurized, no deformities were observed due to the variation in membrane thickness. The primary downside is that the actual thickness of the membrane is difficult to determine accurately, complicating precise model predictions. This uncertainty is one of the reasons an tuning parameter was applied to the model.

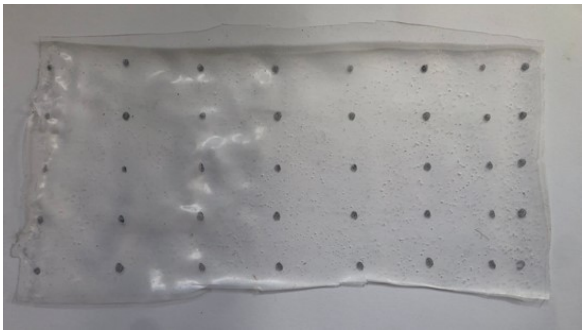

(a) Test piece of silicone with thickness measurements taken. Dots on the silicone are 20 mm apart.

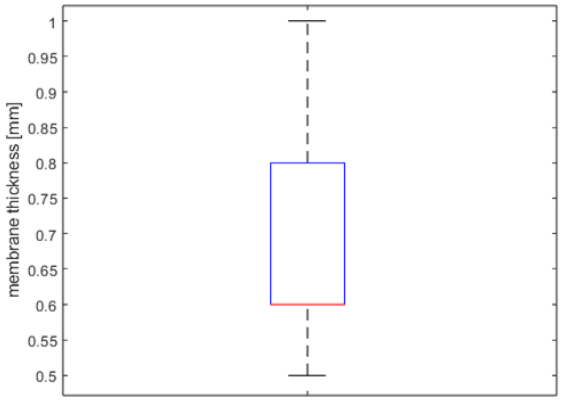

(b) Boxplot of the thicknesses with 40 measurements.

Figure C.23: Silicone thickness measurements and analysis.

Appendix C.2. Hydrostat Assembly

Now that the silicone sleeve is ready, the next step is to pressurize it with water and seal it. The most effective method found was to pressurize the sleeve under a tap before sealing it. Attempting to seal it first and then fill it, such as with a syringe, deemed unsuccessful because the flow rate was insufficient, causing more water to escape than enter at higher pressures. Additionally and most importantly, even a tiny hole in the sleeve made it very difficult to achieve a watertight seal again.

Appendix C.2.1. Sealing Methods

There are various methods to seal the hydrostat after it is pressurized. The exact technique used by commercially available water wigglies is unknown, but it appears they overlap the ends of the sleeve and use a heat seal to melt the ends together. However, it is unclear how this would work with a pressurized silicone sleeve.

Root et al. (1) proposed a method for using silicone glue by first bundling the ends of the sleeve, tying it off to maintain pressure, and then overlapping and gluing the ends together. An attempt to try this method with the silicone glue SIL-POXY proved difficult due to its 5-minute cure time and the challenge of maintaining the sleeve pressurized. Additionally, the glue was highly irritating and dried out quickly, making it difficult to work with.

As a last resort, instead of sealing the ends, the entire end of the sleeve was secured with tie wraps. This method proved highly effective, making the hydrostat extremely watertight. It is also a very easy and forgiving process. This non-permanent solution allows for quick adjustments if the hydrostatic pressure is not as desired, without having to cut it open and lose sleeve length after the glue has cured. The only downside is that the hydrostat is no longer hollow, but this was not an issue for the intended purpose.

Appendix C.2.2. Assembly steps

The method of pressurizing and sealing the sleeve is as follows, and is depicted in Figure C.24:

1. Cut the sleeve to the desired size, leaving enough excess material for tie wrapping.
2. Fold the sleeve onto itself.
3. Prepare a tie wrap and place it over the faucet.
4. Pressurize the sleeve by filling its pocket with water from the faucet, squeezing the sleeve around the faucet. Be sure to first let all the air escape.
5. Once the desired diameter is achieved, lower the tie wrap over the sleeve, release it from the faucet, and quickly tighten the tie wrap. Note that some water will escape, so slightly overfill the sleeve.
6. The hydrostat is finished. For added water tightness, place an additional tie wrap behind the first one.

(a) Step 1: Cut the sleeve to size

(b) Step 2: Fold the sleeve

(c) Step 3: Prepare at the tap

(d) Step 4: Pressurize the sleeve

(e) Step 5: Tie off the sleeve

(f) Step 6: Finalized hydrostat

Figure C.24: 6 Step hydrostat assembly

Appendix D. Test Setup

To validate the parametric model, an experimental test setup was designed and built to conduct three types of tests: a pull test, measuring the holding force as a function of the swallow distance; a push test, measuring the axial force as a function of the swallow distance, and a tensile test, determining the stress-strain relationship of the silicone by measuring axial force as a function of the material elongation. These tests can be performed in one setup, as for all tests, both axial force and distance are measured. Figure D.25 shows the schematic depiction of the setup, which consists of two main parts: the motion stage and the measuring stage.

Force measurement is conducted with a load cell on the measuring stage, while actuation and distance measurement are performed on the motion stage.

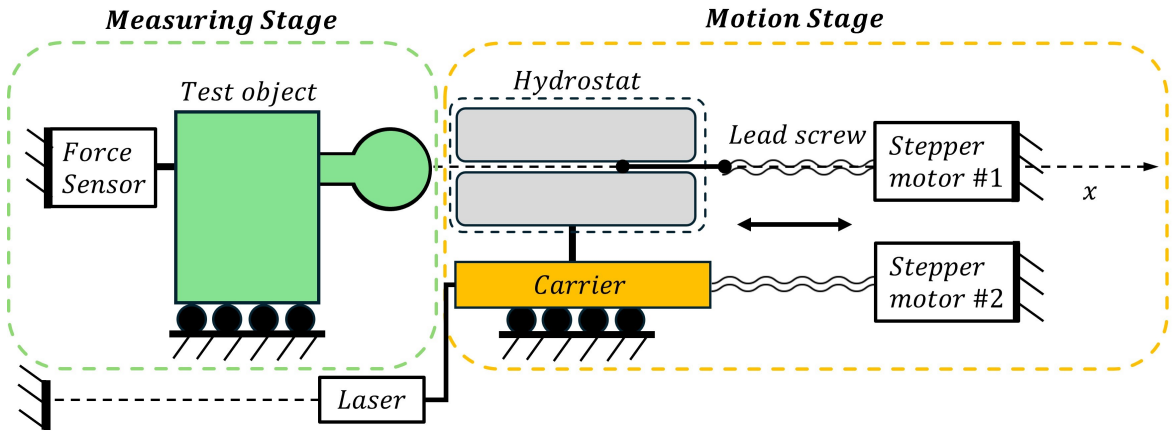

Figure D.25: Schematic depiction of the test setup with the motion stage in orange and the measuring stage in green. The hydrostat is suspended in a carrier on a linear guide. Lead screws operate the inner and outer membranes of the hydrostat. The test object is positioned on a near-zero friction linear guide and is connected to the load cell.

Appendix D.1. Motion Stage

The objective of the motion stage is to construct a 2-degree of freedom (DOF) rig capable of actuating the inner and outer membranes of the hydrostat gripper independently in a purely linear motion. Additionally, a method to measure the actuated gripping distance is necessary. To ensure consistent measurements, a homing sequence is utilized to always establish the same zero point, which requires the addition of end-stop sensors. Figure D.26 depicts the entire motion stage.

Appendix D.1.1. Hydrostat Carrier

The carrier, depicted in D.27, is the central component of the motion stage and is fully 3D-printed. Its purpose is to house the hydrostat and actuate its outer membrane along a purely linear motion. Additionally, it must accommodate different sized hydrostats and allow for quick and easy changes without disassembling the entire motion stage.

As shown in D.26, the carrier sits on a linear guide system consisting of THORLABS XE25L225/M optical rails connected to SBR16UU linear bearings, facilitating the linear motion. The carrier slides easily on these rails, though they do not have zero friction. However, because the motion and measuring stages are decoupled, this does not affect the measurements.

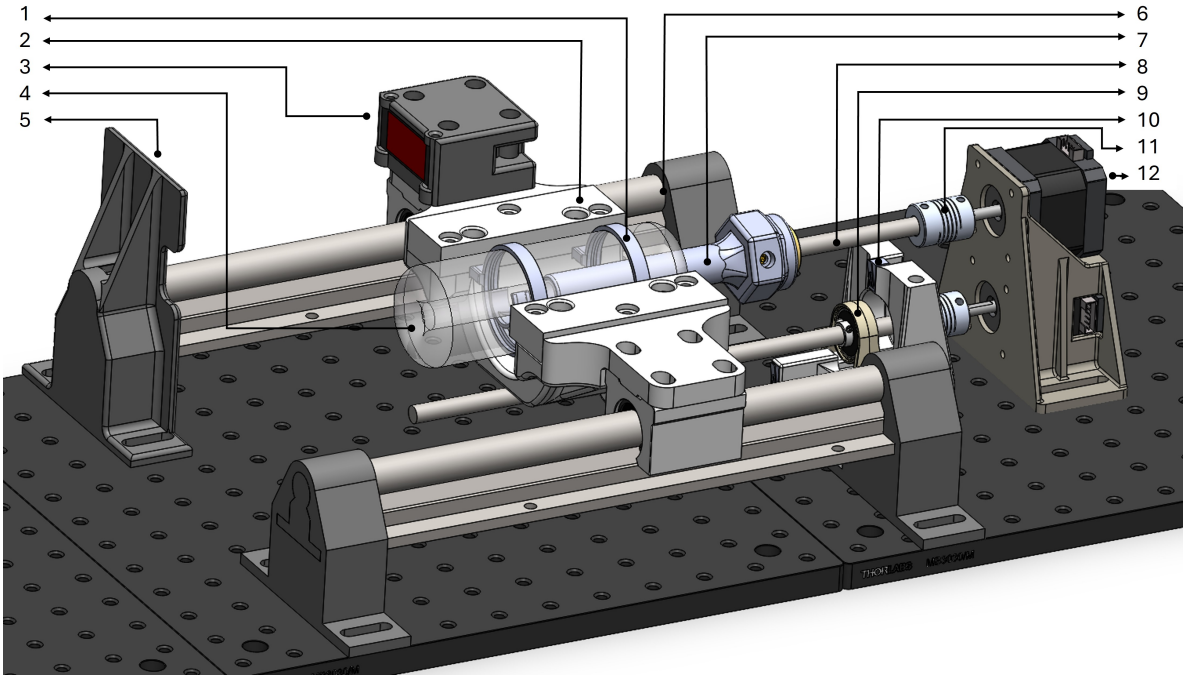

Figure D.26: Motion stage components: 1: Compliant hydrostat clamp, 2: Hydrostat carrier that actuates the outer membrane, 3: ILD1420-100 laser, 4: Hydrostat, 5: Measurement board for laser, 6: Linear guide system comprised of THORLABS XE25L225/M optical rails connected to SBR16UU linear bearings, 7: Actuation pen that actuates the inner membrane, 8: Lead screws for actuation, 9: KP08 bearing, 10: Microswitch end stop, 11: flexible motor coupling, 12: NEMA-17 stepper motor.

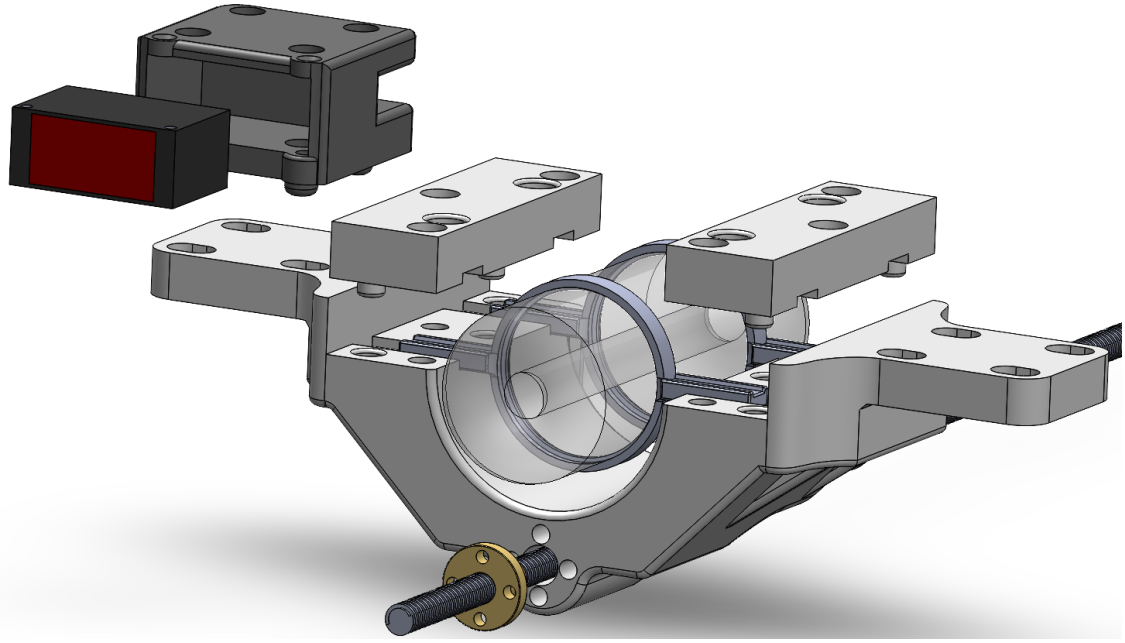

Figure D.27: Exploded view of the hydrostat carrier, showing the hydrostat secured with o-ring shaped compliant clamps tightened with blocks. The laser is additionally mounted on the carrier.

It is crucial that the center of the hydrostat remains at the same height, regardless of its diameter. This is achieved by clamping the hydrostat in a compliant o-ring-shaped clamp. The clamp's diameter is critical; too tight a fit can squeeze the hydrostat and alter its performance, while too loose a fit can allow the hydrostat to

slide out when the holding force exceeds the clamping force. Various clamp diameters were 3D-printed, and using a slightly smaller diameter as the back clamp proved effective in keeping the hydrostat in place without affecting performance.

(a) 3D printed hydrostat clamps in various diameters.

(b) A closeup of a hydrostat clamp.

Figure D.28: 3D printed hydrostat clamps.

Two blocks are inserted over the clamps and secured to the carrier using M4 brass inserts. Additional screws tighten the clamps, allowing for minor adjustments to the hydrostat position. This system ensures a secure clamping solution for different hydrostat sizes while also facilitating easy removal.

A lead screw nut can be screwed to the bottom of the carrier, enabling actuation by the stepper motor through a lead screw.

Appendix D.1.2. Actuation pen and nut

To actuate the inner membrane of the hydrostat, a pen-shaped object is designed and depicted in D.29. This pen attaches to the loose silicone at the end of the hydrostat by placing the silicone into the half-open compliant circle and clamping it together with a tie wrap. The pen connects to a 3D printed nut that slides over the pen and they are jointed together using M4 bolts. The nut is attached to the lead screw via a lead screw nut. This design allows the pen to be attached to the hydrostat outside of the rig and assembled as one piece. Again, facilitating convenient disassembly of the hydrostat.

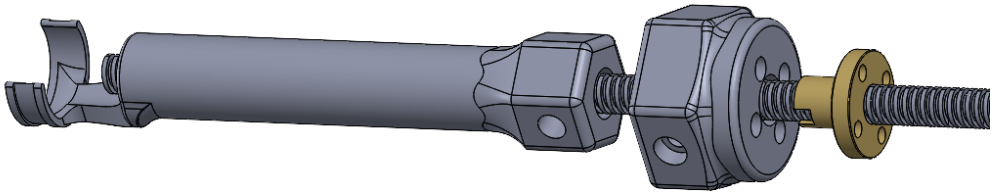

Figure D.29: Exploded View: Disassemblable actuation pen and nut with lead screw.

Appendix D.1.3. End-stop Mount

To enable the homing sequence, end-stops are installed using standard 3D printer sensors, compatible with UGS software. A small 3D-printed mount holds the sensors with a press fit. The lead screw nuts on both the carrier and the pen hit these sensors, resetting their positions within UGS. A bearing is screwed on the mount, with the carrier's lead screw passing through and attaching to the bearing with an adjusting screw. This ensures the spring-like flexible motor coupling doesn't interfere with the actuated distance.

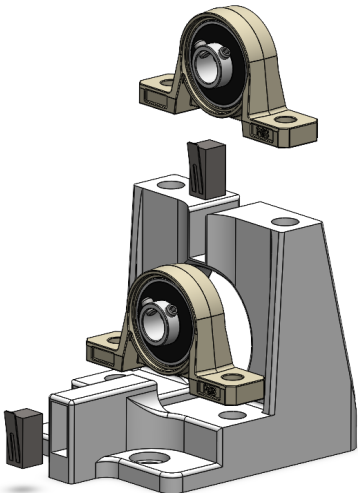

Figure D.30: Exploded view: Mount for bearings and end-stops.

Appendix D.2. Measuring Stage

The objective of the measuring stage is to accurately measure the axial force exerted on the test piece by the hydrostat gripper, without interference from other forces. The stage must allow for easy switching of various test pieces and provide adjustability to ensure the test piece is positioned exactly in the center.

Appendix D.2.1. Object Mount

Figure D.31 depicts the measuring stage, which comprises an RTS-2065 linear guide system allowing pure translational motion with negligible friction. A connection mount is installed to provide sufficient height for the carrier to pass beneath the test object. The load cell is secured to the back with an M3 bolt. On top of the mount is a mounting piece for the test objects, featuring a pointy end for attaching different test pieces. The test pieces are secured to the mount with an M4 bolt. The object mount is connected to the connection mount using M5 bolts, with height adjustment plates placed between them for fine-tuning the height. Additionally, grooves in the object mount allow the M5 bolts to slide, enabling left-to-right positional adjustments. Lastly, the load cell is attached to the load cell mount.

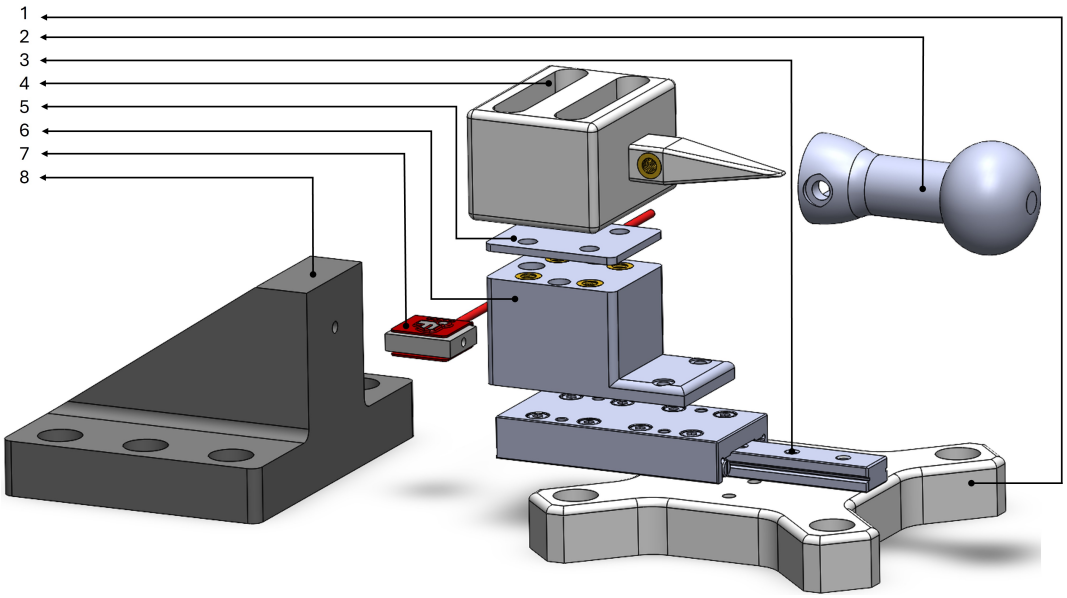

Figure D.31: Exploded view of the Measuring stage: 1: Connection plate for the linear guide, 2: Test object, 3: RTS-2065 Linear guide system, 4: Object mount, 5: Plate for height adjustment, 6: Connection mount, 7: Futek LSB200 load cell, 8: Load cell mount.

Appendix D.2.2. Test pieces

Various test pieces were designed and 3D printed. They are designed in such a way that they easily can be attached to the object mount via a m4 bolt, that can be screwed into the brass insert that is pressed into the object mount as can be seen in D.31. Figure D.32 depicts the various test objects that were used.

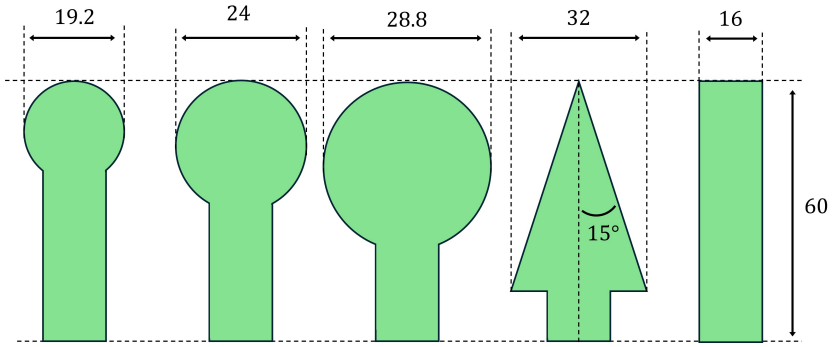

Figure D.32: Test Objects: from left to right; 80% sphere, 100% sphere, 120% sphere, cone, cylinder. All values are in *mm*.

Additionally, the stress-strain curve of the silicone had to be measured. A tensile tester rig, depicted in D.33, was designed and 3D printed. It can be screwed into the object mount on the one side, and can be hung in the hydrostat carrier on the other side. The silicone test pieces are attached to the tester by clamping it with a 3D printed beam that can be screwed into the tester.

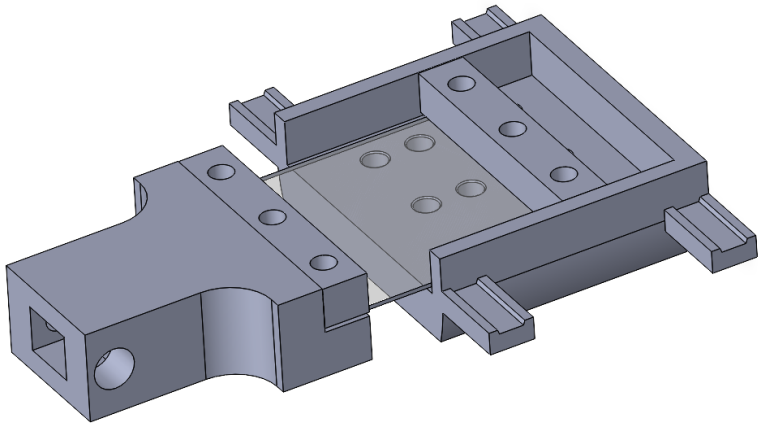

Figure D.33: Tensile tester setup. The silicone is clamped in both pieces, which can be attached to the test mount and the hydrostat carrier.

Appendix D.3. Assembly

The entire rig is assembled onto a THORLABS MB2020/M aluminum breadboard with M6 bolts, as shown in D.35. To aid alignment, specific 3D-printed parts hook onto the breadboard's sides, ensuring precise positioning. These parts help align the linear guides to be parallel with each other, and ensure the hydrostat carrier, bearing mount, and motor are perfectly aligned. Crucially, they also ensure the load cell is perfectly parallel to the RTS-2065 linear guide's movement, preventing angle measurement errors. Figure D.34 showcase some of the assembly blocks used.

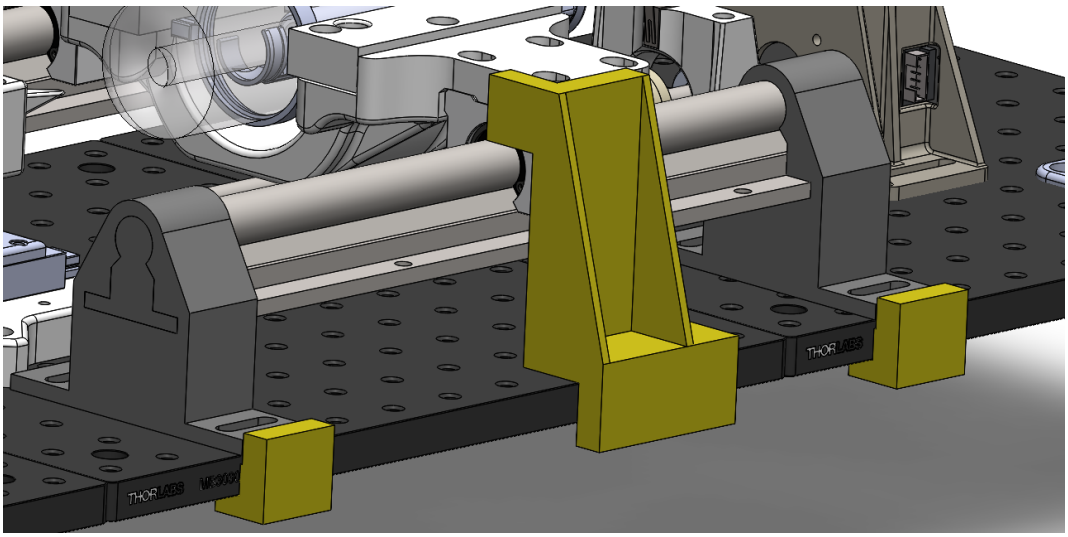

Figure D.34: Examples of the assembly blocks for the linear guide and hydrostat carrier, depicted in yellow.

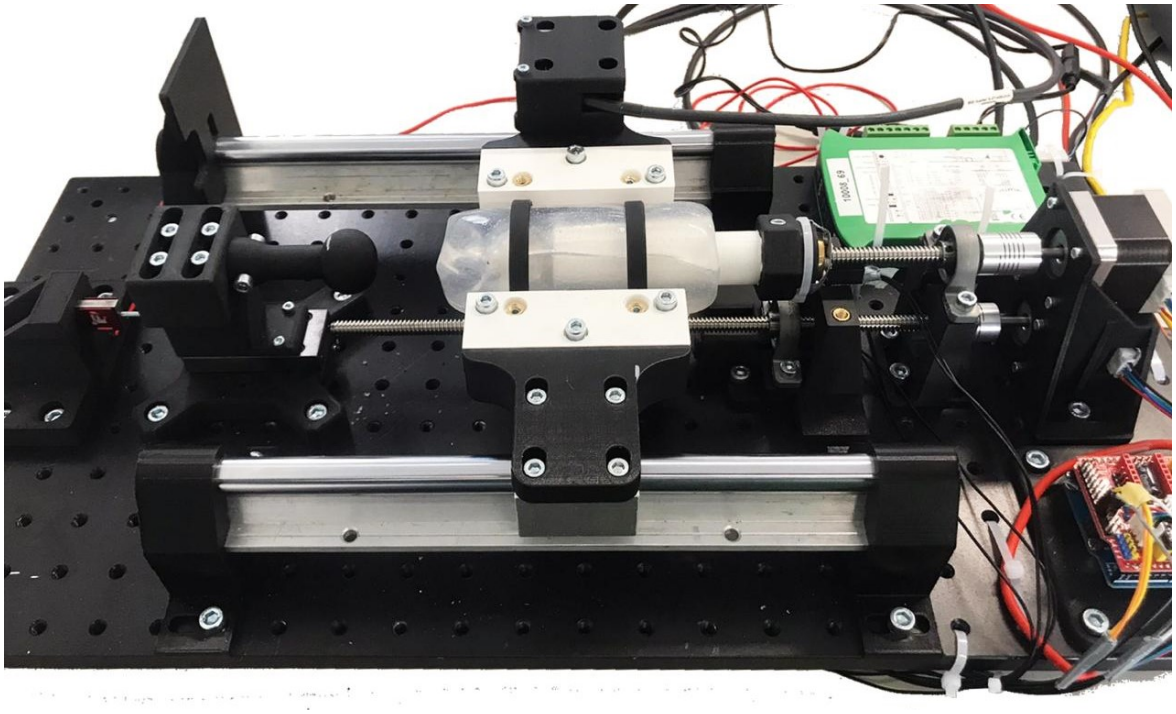

(a) Angled view of the test setup.

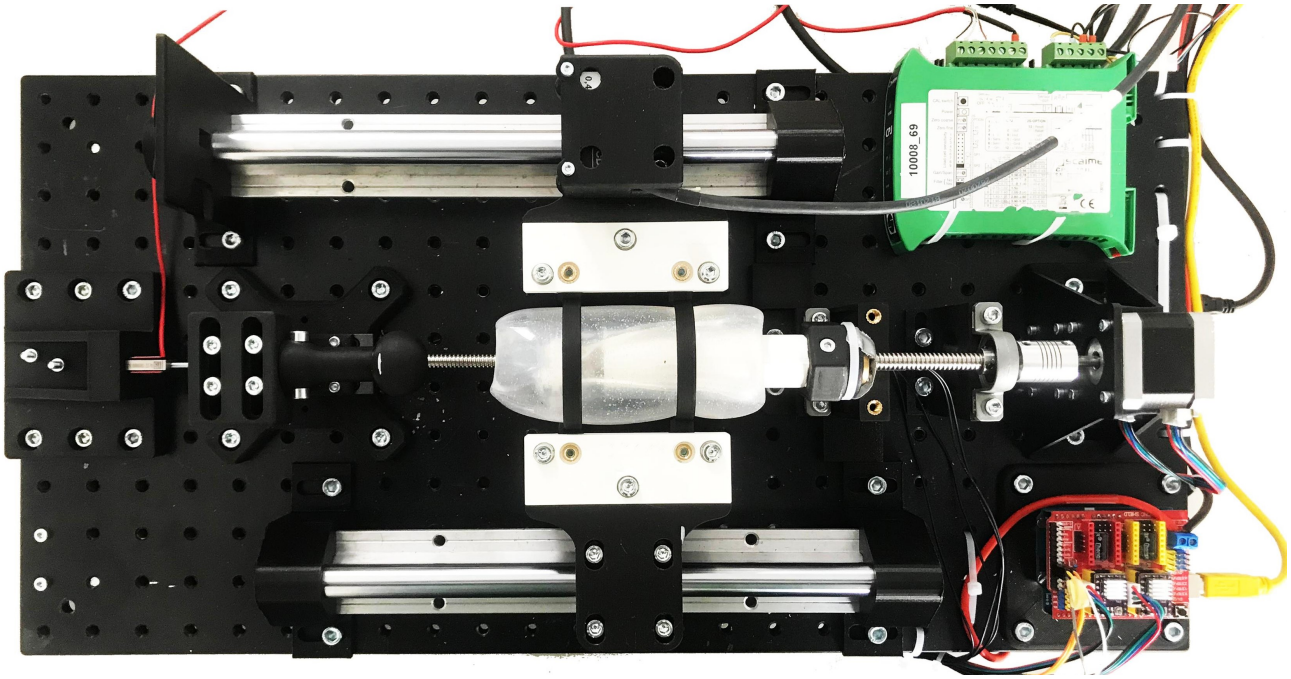

(b) Top view of the test setup.

Figure D.35: Photos of the test setup from different angles.

Appendix D.4. Actuation

For the actuation, two NEMA-17 motors with a maximum torque of 4.08 $kg.cm$ are used. They are controlled by an Arduino Uno with a GRBL Shield. The motors are mounted on 3D-printed brackets and connected to the lead screws via flexible couplings.

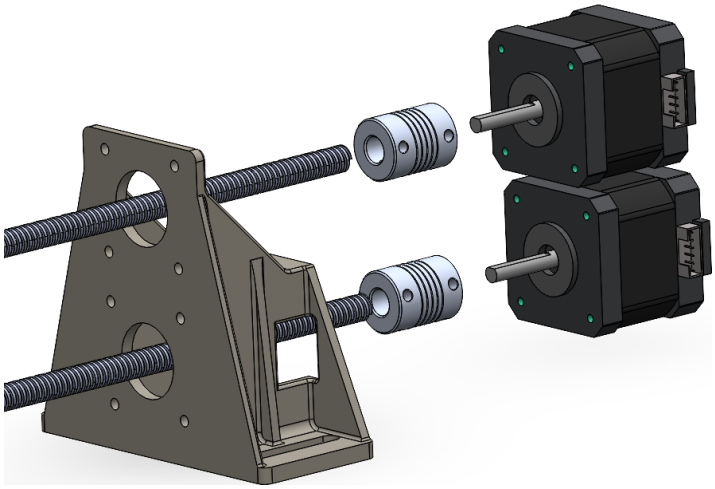

Figure D.36: Exploded view: two NEMA motors on a mount with flexible coupling and lead screw.

Appendix D.5. Measuring

The measuring devices are connected to a NI USB 6008 I/O device, which is connected to the laptop via a USB port and read out using LabView.

Appendix D.5.1. Laser

A laser is used to measure the actuated distance, rath er than calculating it using the stepper motors, as they require calibration and may skip steps when overheated. The actuated distance is measured by a Micro-Epsilon ILD1420-100 laser, which is mounted on top of the carrier and projects its beam onto a modified mount of the linear guide system. This laser has a resolution of 0.136 mm.

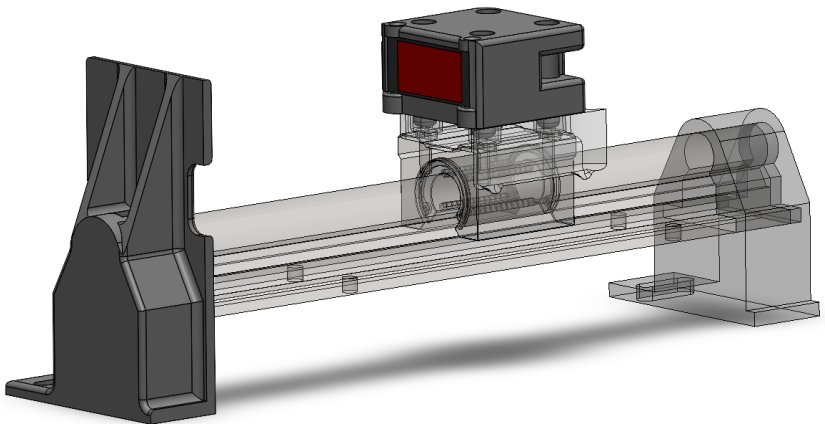

Figure D.37: Laser mounted on the hydrostat carrier, projecting onto a board.

Appendix D.5.2. Load Cell

The axial force is measured using a Futek LSB200 load cell, calibrated at 60N with 1000 steps, providing a resolution of 0.06N.

Appendix E. Testing Procedures

Appendix E.1. Programming

The testing phase utilized two programs: LabView and Universal Gcode Sender (UGS). UGS was employed to actuate the motors, while LabView was used to read the measuring devices.

UGS, commonly used for 3D printers, integrates easily with Arduino and provides a simplified and intuitive interface for operating stepper motors. It also includes a homing sequence for setting a definitive zero point.

To use UGS, you need an Arduino and a GRBL shield. The GRBL software can be downloaded from GitHub and uploaded to the Arduino.

A minor code adjustment is necessary for the homing sequence, which by default homes all three axes. Since only two axes are used, the code must be modified to prevent the homing sequence from indefinitely trying to home the third axis.

In the `config.h` file, change the homing sequence at line 77 to the following:

```
1
2 // NOTE: Defaults are set for a traditional 3-axis CNC machine.
3 // #define HOMING_CYCLE_0 (1<<Z_AXIS)
4 #define HOMING_CYCLE_0 ((1<<X_AXIS)|(1<<Y_AXIS))
5 // #define HOMING_CYCLE_2
```

Within UGS, the stepper motors and end-stops need to be calibrated. This is easily done using the ”Setup wizard” under the ”Machine” tab. Once everything is set up, macros can be used to define the starting points of the measurements. This ensures that after the homing sequence, the hydrostat can be placed in the same spot each time.

Appendix E.2. Testing actions

To achieve accurate measurement results, the process was conducted in a structured manner comprising three phases: Initialization, Setup, and Measuring.

Appendix E.2.1. Initialization

- Provide power to the load cell and to the laser. This is done 20 minutes prior to testing, so the load cell can come up to temperature.
- Connect the NI USB 6008 I/O and Aruidno Uno to the PC via USB.
- Open LabView en UGS

Appendix E.2.2. Setup

This step is performed once for all measurements to ensure consistent results, as movement of the hydrostat with respect the carrier can influence the results.

- Attach the pen to the hydrostat with an tie wrap.
- Place the hydrostat in the carrier and tighten the clamps. Ensure that both the inner and outer membranes can travel 50 mm to the starting point for the pull test.
- Attach the pen to the lead screw nut.
- Find the starting point:
  - Perform a homing sequence so we start from zero.
  - Using UGS, move the outer membrane to the tip of the object, as close as possible without applying force to the load cell.
  - Simultaneously, move the inner membrane towards the object and the outer membrane away from the object, minimizing the distance between the pen and the object without over-actuating and piercing the hydrostat.
  - Finalize the initial position, ensuring no pre-load on the load cell, and add the coordinates to the UGS macros for easy reference.

Appendix E.2.3. Measurements

With the hydrostat set up, the measurements phase can begin. Three different tests were conducted: push, pull, and tensile tests. Before testing, calibrate the load cell to account for temperature variations. All measurements are labeled with hydrostat dimensions (radius and thickness), object, swallow distance, and test type. For example, "R16t14Dummy00_50_Push" indicates a hydrostat with a 16mm radius and 1.4mm thickness, tested on a cylindrical object with a 50mm push test.

Begin by selecting the test object and attaching it to the object mount. Note that the actuated distances are twice the swallow distance when only one membrane is actuated. Positive direction actuation is towards the object.

Push Test This test is conducted in a single measurement with a 50mm swallow distance.

1. Perform the homing sequence.
2. Go to the starting position.
3. Start the measurement in LabView.
4. Actuate the outer membrane in positive direction for 100 *mm* at 100 mm/min.
5. Stop the measurement in LabView.
6. Actuate the outer membrane in negative direction for 100 *mm* at 500 mm/min.
7. Perform the homing sequence and for more measurements restart from step 2.

Pull Test This test is done separately for each swallow distance.

1. Perform the homing sequence.
2. Go to the starting position.
3. Actuate the outer membrane in positive direction for 2*desired swallow distance *mm* at 100 mm/min. This slow speeds ensures that the stepper motors don't skip a step.
4. Start the measurement in LabView.
5. Actuate both the outer and inner membrane in negative direction for 1*desired swallow distance at 100 mm/min.
6. Stop the measurement in LabView.
7. Perform the homing sequence and for more measurements restart from step 2.

Tensile Test This test requires a different setup.

- position the tensile tester so that the material is almost but not stretched.
- Attach this position to a macro.
- Start measurement

1. Start the measurement in LabView.
2. Actuate the motor of the outer membrane in negative direction for as far as possible at 50 mm/min.
3. Stop the measurment in LabView.
4. actuate the motor in positive direction and go back to the initial position at 100 mm/min. This slow speeds ensures that the stepper motor doesn't skip a step.

Appendix F. Tensile Test Results

The Young's modulus of SORTA-CLEAR silicone is not listed on the manufacturer's website, so an experiment was conducted to obtain the non-linear stress/strain curve of the material. A function can then be fitted to this curve for use in the parametric model.

Appendix D.2.2 shows the rig used for measurements. A silicone piece with dimensions 75x59x0.9mm, cut from an unused sleeve, was used for the experiment. Care was taken to ensure the piece had a uniform thickness throughout.

The measurement procedure was as follows: The test piece was secured in the tensile tester by clamping the edges. The rig was positioned to avoid any preload, ensuring the material was not prestretched. The new stretchable length was measured after clamping, resulting in a new dimension of 59x59x0.9mm. The test piece was then stretched to 210% of its original length at a constant speed of 50mm/min and the traveled distance and pulling force was recorded. Two measurements were conducted in total.

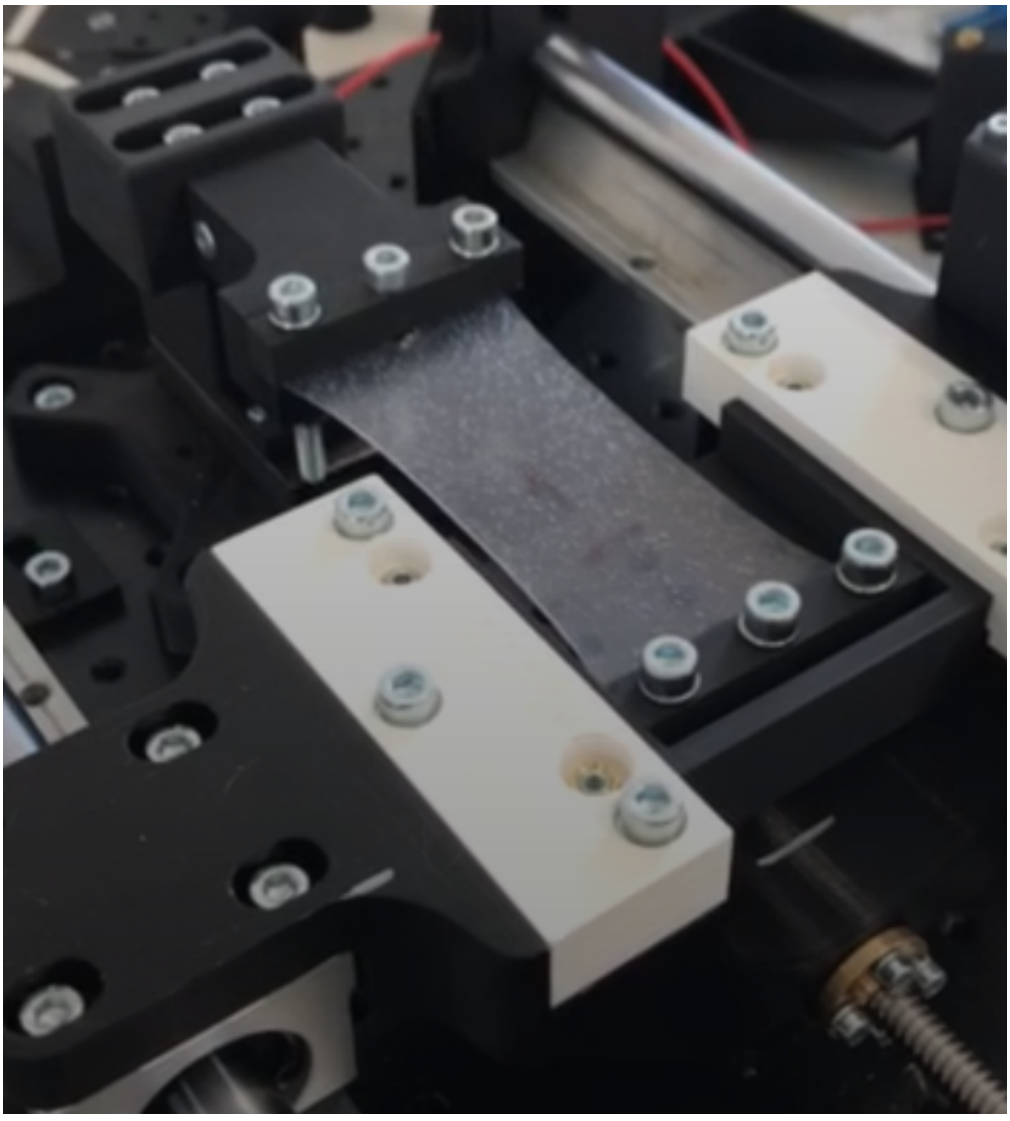

Figure F.38: Tensile test of a piece of silicone. As the silicone is stretched, it takes on an hourglass shape, indicating a change in the cross-sectional area.

Figure F.38 shows the test being conducted. It is evident that as the test piece is stretched its cross-sectional area A changes. To account for this change in area, the true strain and stress are used instead of engineering strain and stress. The engineering strain ε_e and stress σ_e, as well as the true strain ε_t and stress σ_t, can be calculated as follows (9), (10):

$$\varepsilon_e = \frac{L - L_0}{L_0} \tag{F.1}$$

$$\sigma_e = \frac{F}{A_0} \tag{F.2}$$

$$\varepsilon_t = ln\,(1 + \varepsilon_e) \tag{F.3}$$

$$\sigma_t = \sigma_e\,(1 + \varepsilon_e) \tag{F.4}$$

From the two measurements, the true stress and strain were calculated, and their mean was taken. Figure F.39 plots the true stress/strain curve and its derivative, Young's modulus/strain. A 6th order polynomial is used to approximate the Young's modulus curve for the model.

The figure shows clear non-linear behavior, with the Young's modulus increasing by 75% at a 0.75 strain. However, the working strain range of the hydrostat is between 0.4 and 0.7 mm/mm, resulting in an increase of 40%. For simplicity of the model, a constant value of 0.6 MPa could be used, which would give a fine approximation.

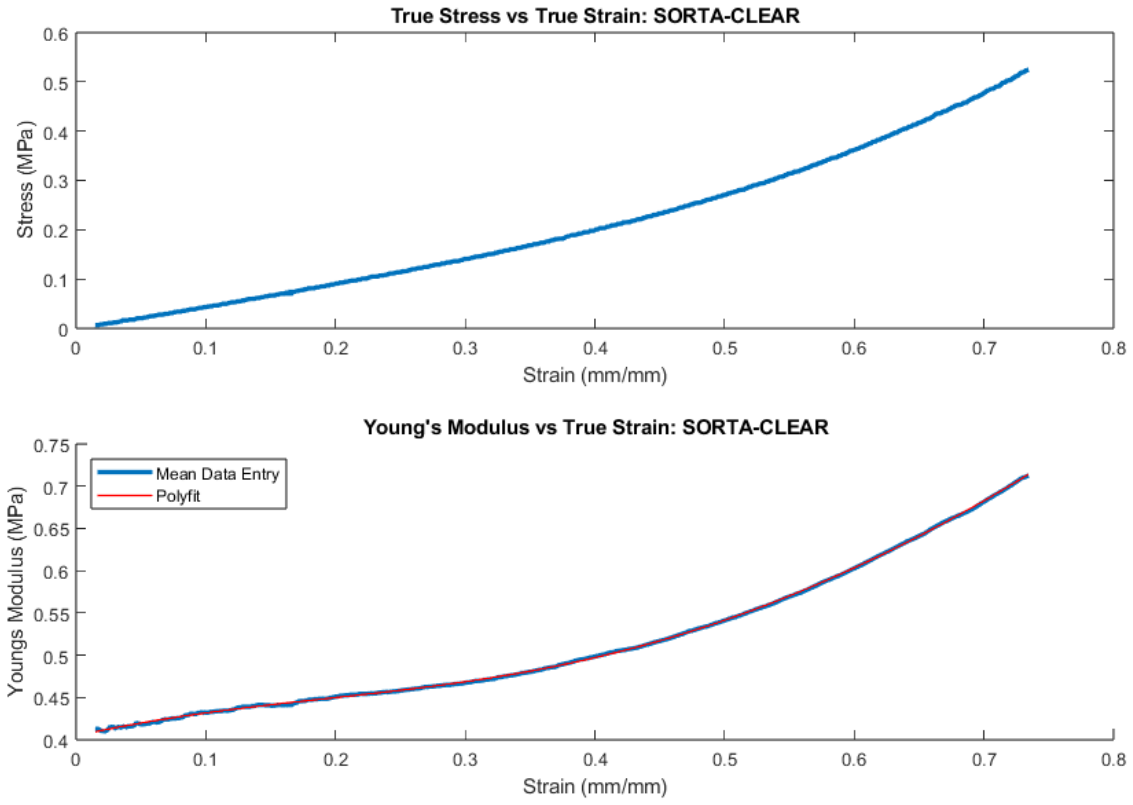

Figure F.39: Stress/strain and its derivative Young's modulus/strain, demonstrating clear non-linear behavior. The Young's modulus increases by 75% at a 0.75 strain.

Appendix G. Hand-held Device

For initial testing of the hydrostats, a hand-held gripper casing was designed. The design required two main parts: actuation for the inner and outer membranes.

For the inner membrane, a simple pen design was used. This design was a precursor to the pen used in the test setup and relied on the friction force between the hydrostat and the pen to stay in place.

The outer membrane underwent several iterations. The first design was inspired by (11), which featured a straight casing. This initial attempt showed that as the hydrostat engulfs an object and its radius increases, the solid casing restricted expansion, causing distortion at the opening and resulting in an irregular force-displacement relationship.

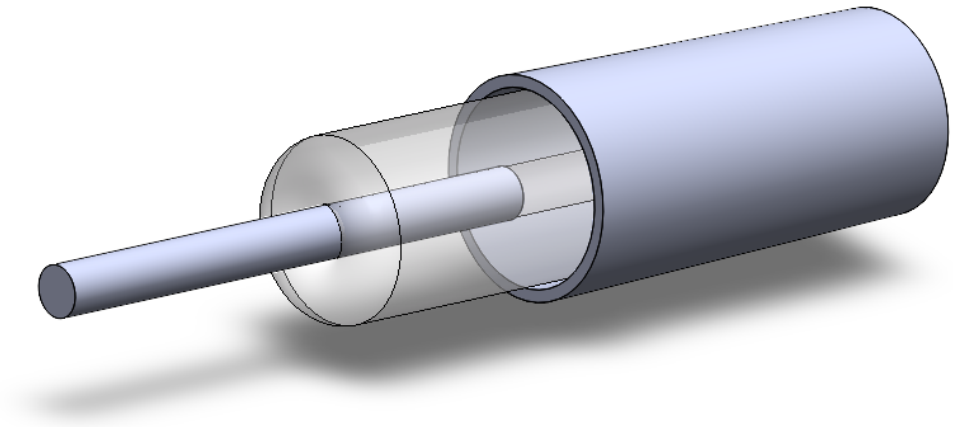

Figure G.40: Hand-held design #1: A cylinder casing.

To address the distortion issues, a second design was proposed featuring a compliant casing that stretches with the hydrostat. While this approach resolved some distortion problems, it introduced additional normal force on the object due to the spring-like behavior of the casing. This hindered the ability to grip large items, as the compliant casing required extra force to further open the hydrostat.

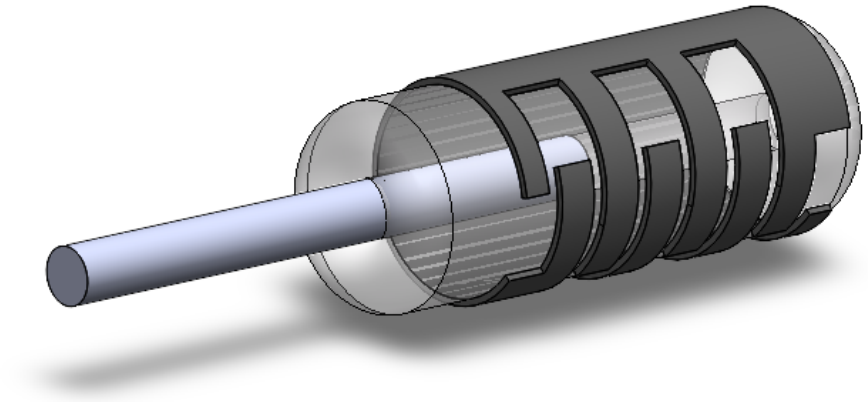

Figure G.41: Hand-held design #2: A compliant cylinder casing.

A third design was proposed, similar to the hydrostat carrier in the test setup. This design uses two rings to close around the hydrostat instead of covering its entire exterior, allowing the hydrostat to expand freely except where the rings are positioned, which had minimal impact on its force/displacement relationship. Despite the small area of the two rings, they provided sufficient friction force to prevent the hydrostat from being pulled out of the casing when lifting objects up to $40N$. Figure G.43 shows the hand-held casing with a hydrostat of $32mm$ radius, $130mm$ length, and $1.6mm$ thickness, successfully lifting various items of different shapes and materials.

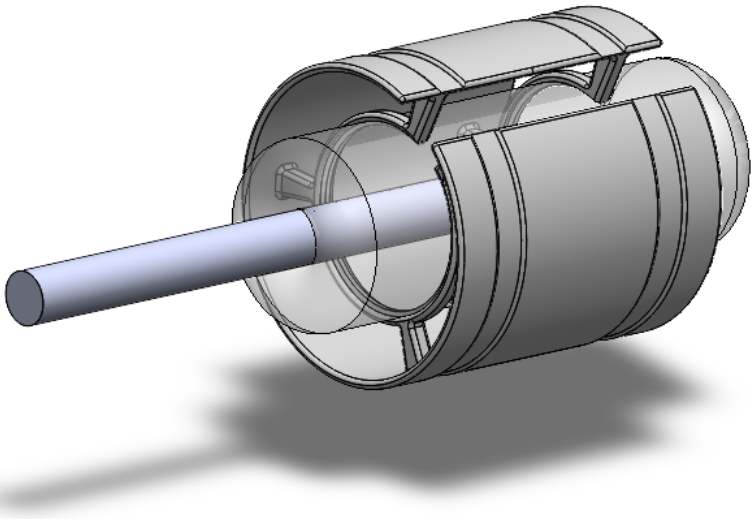

Figure G.42: Hand-held casing design #3: Compliant o-ring casing.

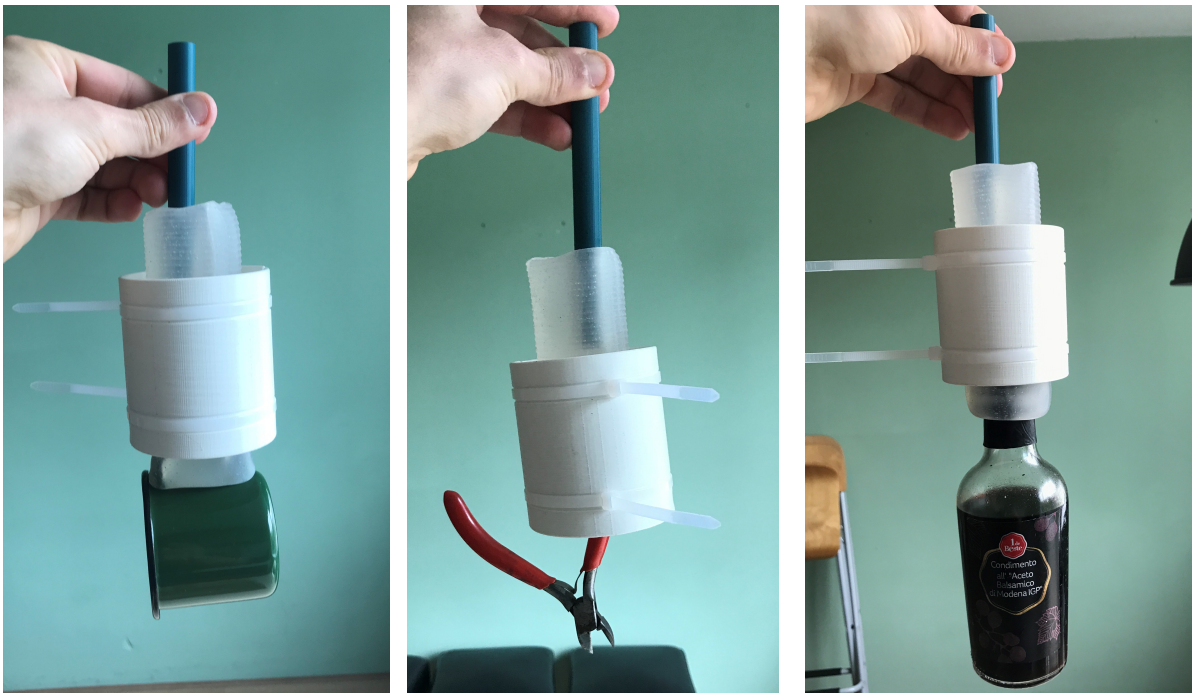

(a) Hydrostat gripper holding a cup.

(b) Hydrostat gripper holding a bottle.

(c) Hydrostat gripper holding a bottle.

Figure G.43: Hand-Held hydrostat gripper gripping various items.

Appendix H. Textured Hydrostats

To increase the holding force of the hydrostat gripper, rather than changing its dimensional or material parameters, the focus was on increasing the friction coefficient by adding textures to the sleeve. Silicone proved to be exceptional at replicating even the smallest details from the molds used, making it ideal for this intended purpose.

Appendix H.1. Texture Selection

In everyday life, textures are ubiquitous and serve to increase friction (12). Examples include the soles of shoes, bike and car tires, and utensils. Additionally, many animals utilize textures to enhance their grip on surfaces (13). These textures are specifically designed to improve the ability to stick to objects. Inspired by these natural and engineered solutions, textured surfaces were explored for the hydrostat gripper to enhance its holding force by increasing the friction coefficient.

Textures can be categorized into shapes and patterns, with shapes being either embossed or debossed. This investigation focused on different shapes while maintaining consistent patterns or those best suited to the shapes. For initial testing, various simple shapes were selected: triangle shapes mimicking snakeskin (14) in both debossed and embossed forms; a dotted pattern similar to a drill handle, embossed; slit shapes inspired by tire sipes (15), (16), debossed; and a full ring resembling seal rings to enhance potential vacuum force observed during testing.

Appendix H.2. Manufacturing

To manufacture these textures, molds needed to be created. Using the existing PVC pipe setup, a simple 3D-printed skin was made to slide over the PVC pipe. Figure H.44 shows the printed skin on the PVC pipe. This technique allowed for easy modeling of textures in SolidWorks and quick prototyping. A challenge was ensuring a tight fit to prevent fluid silicone from seeping underneath the mold, which would make removing the sleeve difficult. Figure H.45 depicts some of the modeled molds.

Figure H.44: PVC pipe with several textured molds: debossed triangle shape, debossed dotted shape, and embossed triangle shape.

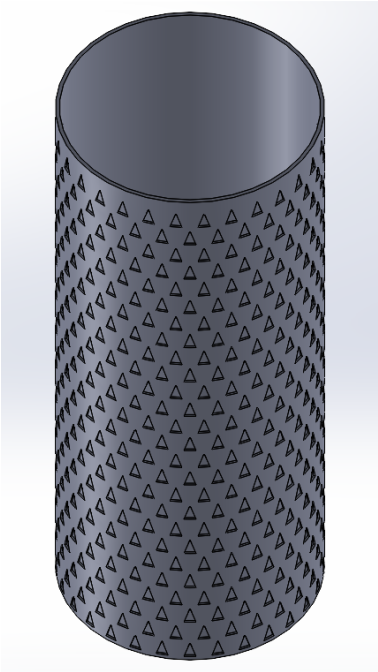

(a) Debossed triangle shape mold.

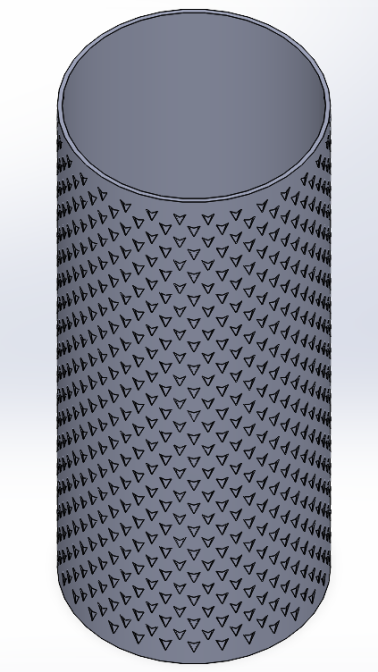

(b) Debossed arrow shape mold.

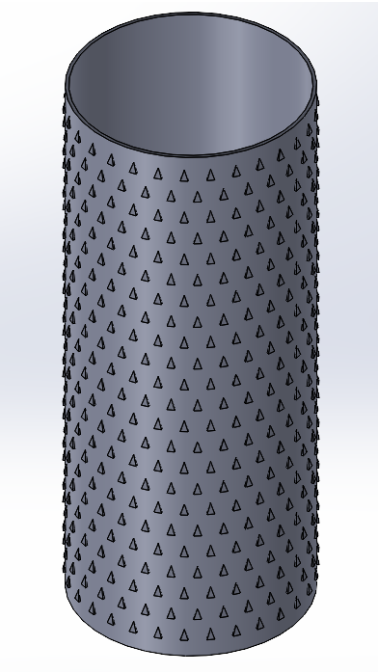

(c) Embossed triangle shape mold.

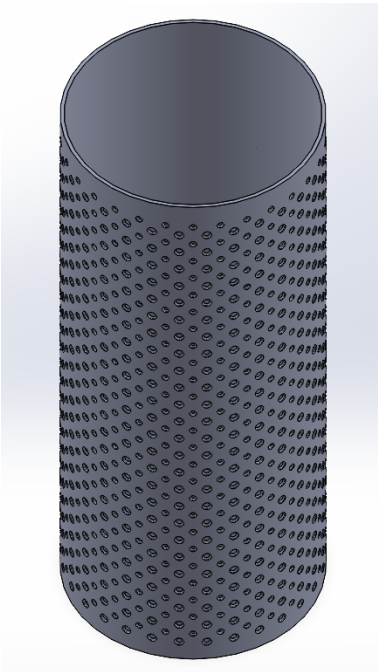

(d) Debossed dotted shape mold.

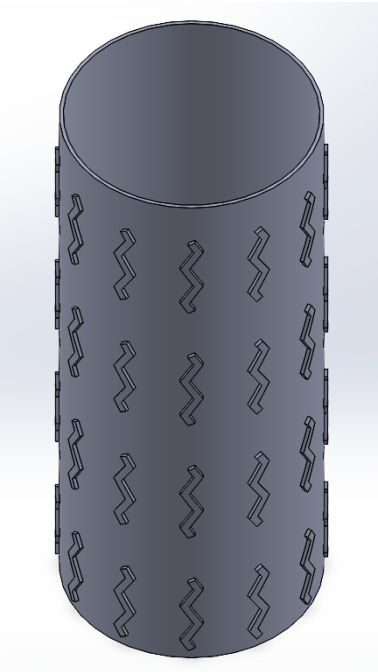

(e) Embossed slits shape mold.

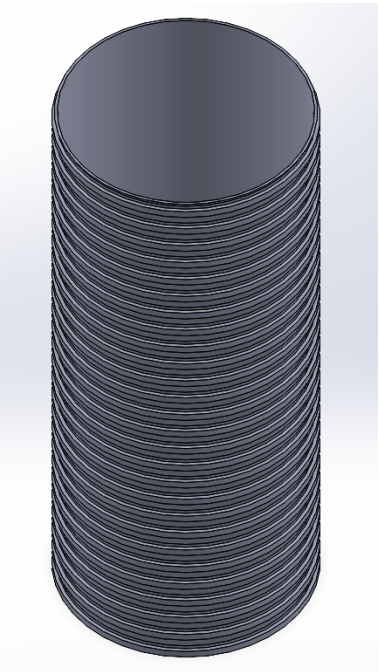

(f) Embossed seal ring shape mold.

Figure H.45: Various texture shape molds

The manufacturing steps are the same as those described in Appendix C.1.3. Various textured molds were placed sequentially on the PVC pipe and manufactured as one piece. This method allowed for easy prototyping and testing of different textures. The process went smoothly, and Figure H.46 shows some of the results. The textures were very pronounced and could be felt by rubbing a finger over the sleeve. However, the debossed textures had a very thin silicone layer, causing them to tear quite easily.

The embossed textured sleeves were the most noticeable to the touch, while the debossed textures blended more with the sleeve. After creating the initial textured sleeves, single sleeves were made with half textured and half non-textured surfaces. These sleeves were pressurized and made into hydrostats, as shown in Figure H.47. But when pressurized, the textures faded slightly due to the sleeve stretching.

(a) Triangle pattern embossed on the sleeve.

(b) Triangle pattern debossed in the sleeve.

(c) Dotted pattern embossed on the sleeve.

(d) Slits pattern debossed in the sleeve.

Figure H.46: Various textured patterns on the silicone sleeves.

Appendix H.3. Texture Testing

No testing was conducted in the test setup; instead, the hand-held device featured in Appendix G was used to pick up various objects. A water-filled bottle was used to determine the maximum holding force. To ensure consistency, the same hydrostat was tested on both the textured and non-textured sides under the same hydrostatic pressure.

Surprisingly, the non-textured side lifted more weight than the textured side across all hydrostats tested. This was likely due to the reduction in radial area caused by the textures, resulting in a lower normal force on the object. It is important to note that these measurements were taken on a smooth bottle, which may not be the best surface for testing textures. Overall, while the ability to add textures is interesting, it does not seem to provide a significant advantage.

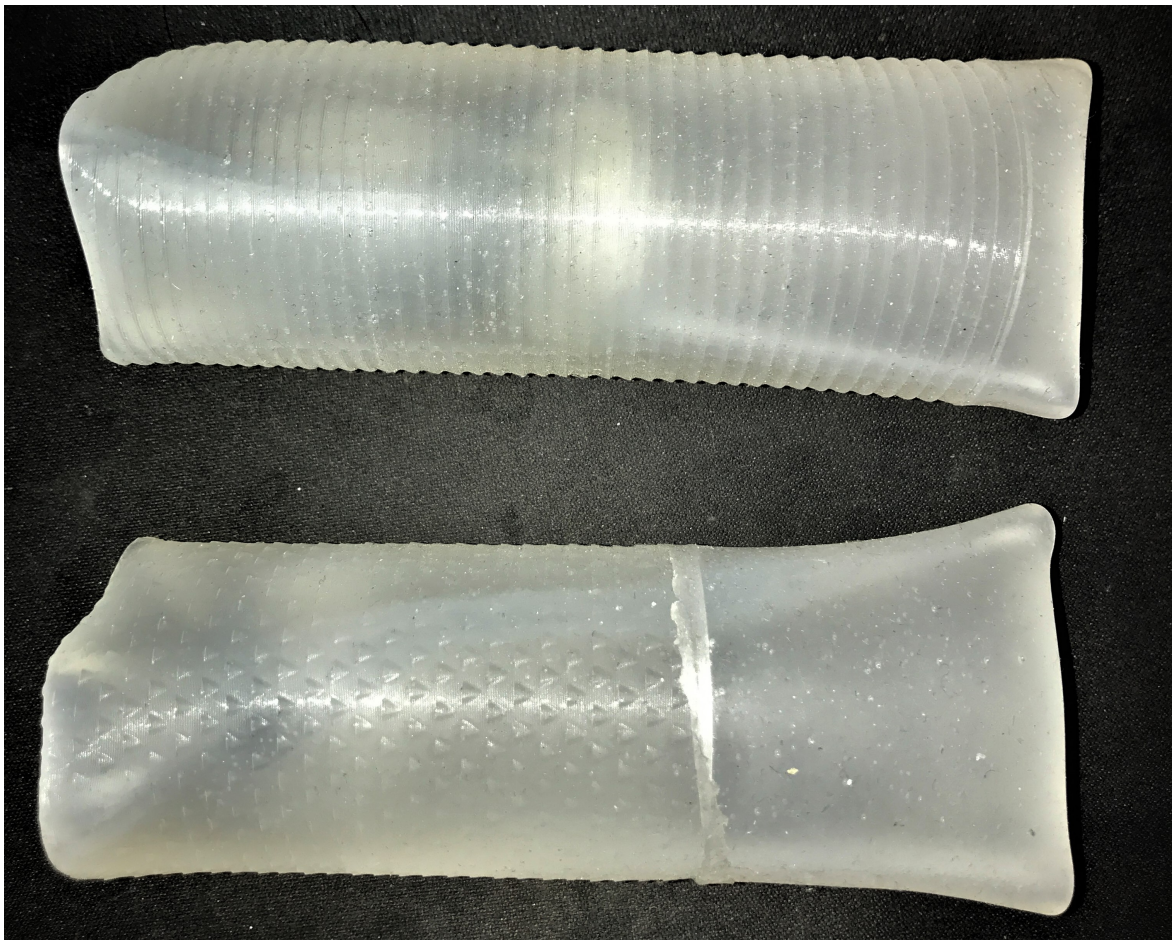

Figure H.47: Pressurized textured hydrostats: the top features the seal ring shape, while the bottom showcases the embossed triangle shape.

Appendix H.4. Future research: Wet Surface Conditions

It was observed that for all sleeves, textured or non-textured, the friction coefficient drastically decreases when the object's surface is wet. Soft robotic grippers are excellent for handling soft materials like food, but many food items have wet surfaces due to condensation from cold storage.

An attempt to solve this issue draws inspiration from the toe pads of tree frogs (13), which can stick to objects even when covered in water. Their toe pads feature a hexagonal pattern, as depicted in figure H.48a, that allows water to sit in the grooves, keeping the hexagonal pads dry and significantly increasing the friction coefficient. Surface tension plays a crucial role, and the benefits of these patterns are heavily influenced by their geometry.

Experiments by Xie et al. (17) showed that the performance of these pads depends on the ratios of their geometric dimensions, with an optimal range of H/L from 0.7 to 0.9 and H/W from 1.0 to 1.8, and a width of 30 μm proving most effective, as depicted in figure H.48d-H.48f. Additionally, Zhang et al. (18) found that an array of top bulges on the pads, as depicted in H.48c, accelerates the breaking of the continuous lubricant film on wet contacts, increasing wet friction under shearing motions.

Unfortunately, this level of detail cannot be achieved with a standard 3D printer, so further testing was not possible. However, given the fine details captured in the previously produced textured silicone sleeves, it is assumed that if a mold of such texture could be created, a silicone sleeve with this texture could be produced.

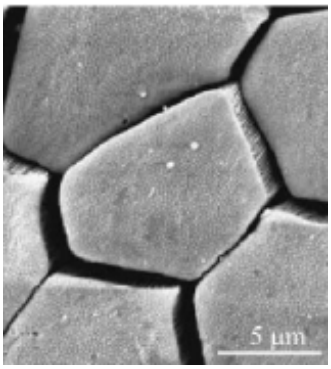

(a) Photo of the frog toe pad.

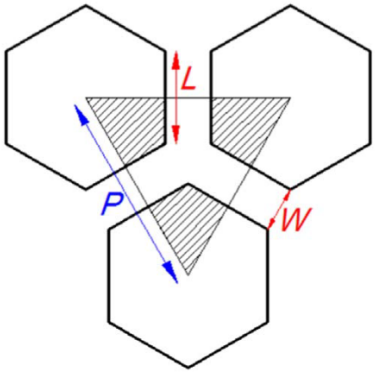

(b) Depiction of the parameters W, L, P.

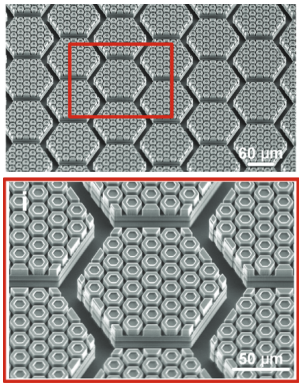

(c) Texture of hexagonal patterns studded with bulges (18).

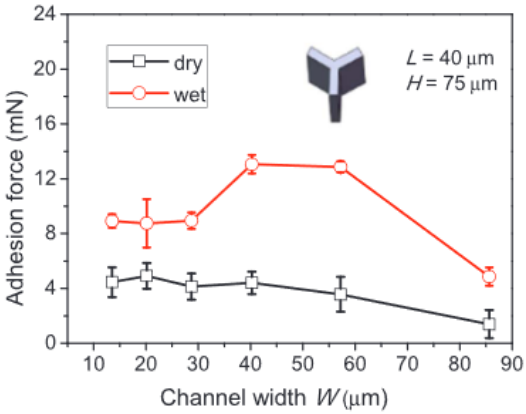

(d) Adhesion force vs. channel width W, L=40μm, H=75μm

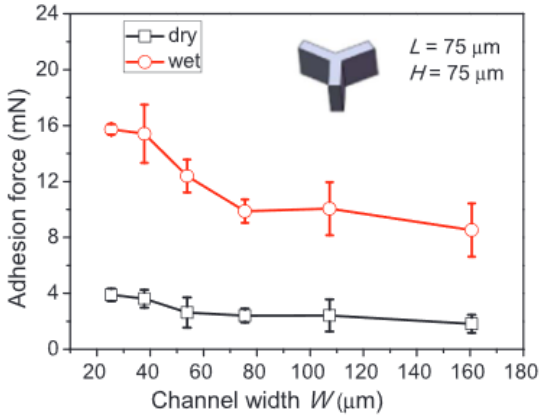

(e) Adhesion force vs. channel width W, L=75μm, H=75μm

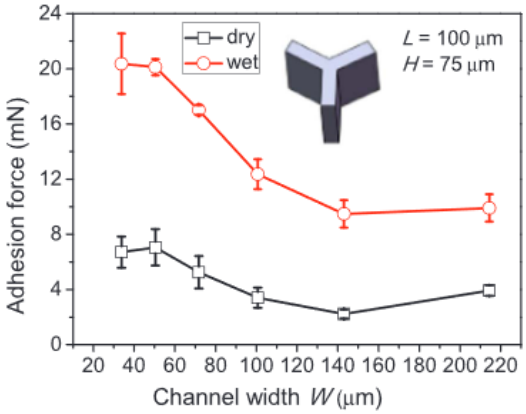

(f) Adhesion force vs. channel width W, L=100μm, H=75μm

Figure H.48: Analysis of the hexagonal-shaped texture found on the pads of tree frogs (17)(18).

References

[1] S. E. Root, D. J. Preston, G. O. Feifke, H. Wallace, R. M. Alcoran, M. P. Nemitz, J. A. Tracz, G. M. Whitesides, Bio-inspired design of soft mechanisms using a toroidal hydrostat 2 (9) 100572. doi:10.1016/j.xcrp.2021.100572.
URL https://www.sciencedirect.com/science/article/pii/S2666386421002873

[2] Numerical integration, page Version ID: 1209747793.
URL https://en.wikipedia.org/w/index.php?title=Numerical_integration&oldid=1209747793

[3] Write a cost function - MATLAB & simulink - MathWorks benelux.
URL https://nl.mathworks.com/help/sldo/ug/writing-a-custom-cost-function.html

[4] Fabrication methods for silicone rubber | silicone dynamics.
URL https://siliconedynamics.net/fabrication-methods-for-silicone-rubber/

[5] Teardrop Heaven, Making DIY homemade balloons.
URL https://www.youtube.com/watch?v=A32qyVqq_44

[6] P. Berthet-Rayne, S. Sadati, G. Petrou, N. Patel, S. Giannarou, D. Leff, C. Bergeles, MAMMOBOT: A miniature steerable soft growing robot for early breast cancer detection PP 1–1. doi:10.1109/LRA.2021.3068676.

[7] SORTA-clear™ series, water clear translucent silicone rubber.
URL https://www.smooth-on.com/product-line/sorta-clear/

[8] B. Reuss, Convert durometer to young's modulus.
URL https://www.cati.com/blog/convert-durometer-to-youngs-modulus/

[9] Engineering strain and true strain.
URL https://courses.ansys.com/index.php/courses/mechanical-strain/lessons/lesson-3-true-strain-and-engineering-strain-2/

[10] Engineering stress/strain vs true stress/strain – yasin ÇAPAR.
URL https://yasincapar.com/engineering-stress-strain-vs-true-stress-strain/

[11] D. Sui, Y. Zhu, S. Zhao, T. Wang, S. K. Agrawal, H. Zhang, J. Zhao, A bioinspired soft swallowing gripper for universal adaptable grasping 9 (1) 36–56, publisher: Mary Ann Liebert, Inc., publishers. doi:10.1089/soro.2019.0106.
URL https://www.liebertpub.com/doi/full/10.1089/soro.2019.0106

[12] H. L. Costa, J. Schille, A. Rosenkranz, Tailored surface textures to increase friction—a review 10 (9) 1285–1304. doi:10.1007/s40544-021-0589-y.
URL https://doi.org/10.1007/s40544-021-0589-y

[13] M. Li, W. Shi, J. Shi, T. Wang, L. Shi, X. Wang, Regulation and control of wet friction of soft materials using surface texturing: A review 11 (3) 333–353. doi:10.1007/s40544-022-0617-6.
URL https://doi.org/10.1007/s40544-022-0617-6

[14] Z. Wang, Q. Fu, R. J. K. Wood, J. Wu, S. Wang, Influence of bionic non-smooth surface texture on tribological characteristics of carbon-fiber-reinforced polyetheretherketone under seawater lubrication 144 106100. doi:10.1016/j.triboint.2019.106100.
URL https://www.sciencedirect.com/science/article/pii/S0301679X19306140

[15] S. Ella, P.-Y. Formagne, V. Koutsos, J. R. Blackford, Investigation of rubber friction on snow for tyres 59 292–301. doi:10.1016/j.triboint.2012.01.017.
URL https://www.sciencedirect.com/science/article/pii/S0301679X12000424

[16] K. Mizushima, T. Nishimura, Y. Suzuki, T. Tsuji, T. Watanabe, Surface texture of deformable robotic fingertips for a stable grasp under both dry and wet conditions 2 (4) 2048–2055, conference Name: IEEE Robotics and Automation Letters. doi:10.1109/LRA.2017.2717082.
URL https://ieeexplore.ieee.org/abstract/document/7953560?casa_token=1RBS-xJhpu0AAAAA:5FviDq7Y2oCN4cw3KfUjasxhC2vpqVbe41CCJmAYgXlE8pD0J9HINXIYiL8h-426u97de5Je

[17] J. Xie, M. Li, Q. Dai, W. Huang, X. Wang, Key parameters of biomimetic patterned surface for wet adhesion 82 72–78. doi:10.1016/j.ijadhadh.2018.01.004.
URL https://www.sciencedirect.com/science/article/pii/S014374961830006X

[18] L. Zhang, H. Chen, Y. Guo, Y. Wang, Y. Jiang, D. Zhang, L. Ma, J. Luo, L. Jiang, Micro–nano hierarchical structure enhanced strong wet friction surface inspired by tree frogs 7 (20) 2001125. doi:10.1002/advs.202001125.
URL https://www.ncbi.nlm.nih.gov/pmc/articles/PMC7578903/